Università degli Studi di Cagliari

DOTTORATO DI RICERCA

in Ingegneria Elettronica e Informatica

Ciclo XXVIII

TITOLO TESI

Optimization of microwave devices

Settore/i scientifico disciplinari di afferenza

ING-INF02

Presentata da:	Marco Simone
Coordinatore Dottorato	Prof. Fabio Roli
Tutor	Prof. Giuseppe Mazzarella

Esame finale anno accademico 2014 – 2015


Optimization of microwave devices

Marco Simone



Abstract

This thesis deals with the optimization techniques for the improvement of the microwave devices performance. In particular, the technique proposed considers the Particle Swarm Optimization algorithm and applies such an algorithm to different devices. Different techniques are developed to connect the optimization with an electromagnetic analysis tool. In the first method the algorithm has been connected to a numerical technique for the evaluation of the device performance (FDFD). The second technique consists on the integration of the algorithm with a 3D Simulation CAD (HFSS, CST). The microwave devices under test are a ridge waveguide (in different configurations), a resonant cavity, a waveguide impedance transformer and an electromagnetic band gap structure. Both the approaches result to be effective for the purpose even in the event that a constraint between conflicting requirements is requested.



Contents

List of Tables

List of Figures

Introduction

As it is well known, the propagation performance of a microwave device is strongly linked to its geometry. The design of complex structures, whose performance depends from several variables, has requested the introduction of techniques which allow to obtain the best solution (that is, the optimal geometry of the structure according to the requests) when the large number of parameters inhibits a direct design or when it's difficult to define an analytic model of the device response. This problem has been overcome with the development of the optimization algorithms. Optimization algorithms allow to define an automatic tool to obtain the best configuration bound to a certain constraint, even if a trade-off between conflicting requests is requested. Among the various classes of algorithms present in literature, the evolutionary computation is one othe most studied and developed, a family of algorithm which allow the parallel computation of several potential solutions. In evolutionary computation, the basic idea is to modify a population of potential solutions to reach the best configuration according the design specifications, which represents the best solution to a problem subjected to a set of constraints. Several optimization algorithms have been realized by the scientific communities, and applied to electromagnetics, like genetic algorithms, evolutionary algorithm or swarm intelligence algorithms. The aim of the optimization is very important in a large variety of fields, like engineering, physics or economy and it is often represented by the search of a global minimum of a proper objective function f defined in the search space W

$$f : W \to \mathbb{R}$$

$$f(\hat{x}) \leq f(x) \quad \forall x \in W$$

f is a fitness function that describe the problem, whose values $f(x_0)$ represent the performance evaluation of any potential solution x_0. To compute this value, a technique of analysis is requested. The basic integration of this two topics (geometry optimization and em analysis) is shown in fig. 1: a optimization tool modify iteratively the population following a set of mathematical formula, the fitness evaluation contains the electromagnetic analysis.

The optimization requests several evaluations of the problem, so the computational load is a crucial issue when it must be chosen the algorithm to adopt, moreover it could find the optimal solution in the fewest number of iterations. Moreover, a suitable parallelization allows

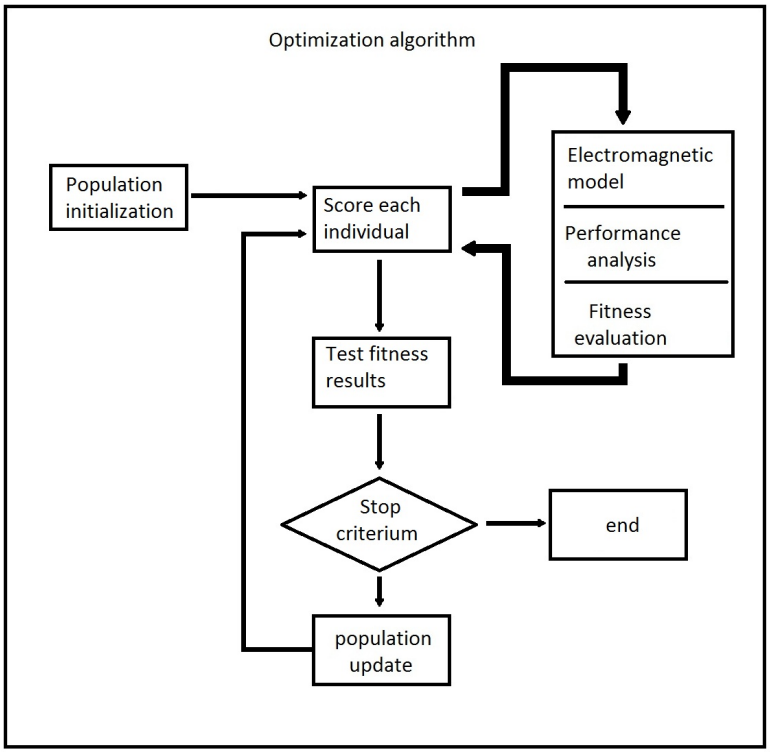

Figure 1: Optimization

to evaluate the fitness of all particles (that is, all the potential solutions of the problem to be optimized) simultaneously. A set of parallel clusters which performs the optimization can significantly reduce the computational time: the slave calculators evaluate the fitness values by implementing and by solving the electromagnetic problem, while the master collects the results relative to all the swarm and implements the optimization algorithm by calculating the parameters required to define the next iteration.

The fitness evaluation is strongly linked to the electromagnetic analysis. To do this, the optimization loop must be integrated with a numerical techniques to solve the Maxwell equations or suitable eigenvalue problems (the most used techniques are FDTD, FDFD, FEM, MoM, etc.) or with a 3D simulation CAD like HFSS, Comsol, CST in order to realize an electromagnetic model of the device to be optimized. The first case is a faster solution respect to the CADS, whereas the CAD allows a higher precision. Some of them, like FDFD, are very efficient in field evaluation. It has a simple implementation and a very easy and fast computation compared to the CAD simulations. Moreover, FDFD technique has been shown to be well suitable to the studied device (ridge waveguide) through proper approximations of the Helmholtz equation and the boundary conditions. By representing the equation in

the different coordinate reference systems according to the geometry under test, the FDFD consists on the direct discretization of the differential eigenvalue problem, which is probably the simplest and most effective strategy to solve such eigenvalue problems.

In this thesis the attention has been addressed of the optimization of microwave devices through the Particle Swarm Optimization. Particle Swarm Optimization is an algorithm with a very simple implementation, which modify its population according to elementary operations and it allows to develop a parallel evaluation of the solutions represented by all the particles of the swarm. The algorithm has been implemented in Matlab and it has been linked to different scripts and CADS to achieve the electromagnetic analysis. In the part 1, the general description of the PSO and some its versions is presented. Moreover, it has been made a view of different applications of the PSO to electromagnetic problems.

In part 2 the optimization of ridge waveguide with contrasting requirements has been faced. The evaluation of the waveguide performance has been achieved through the implementation of a FDFD technique linked to the objective function of the algorithm. Moreover, a 4th-order FDFD method has been designed to evaluate the potential on the transverse section of the waveguide. The method has been implemented for both cartesian and elliptic reference systems, in order to optimized different ridge waveguide geometries.

In part 3, two different solutions of end-launcher for rectangular waveguide have been design. In this project, it has been necessary to apply the optimization to the sizing of a multistep Chebychev transformation trough a combined operation of the PSO written in Matlab and the HFSS software, the two software communicate each other through Visual Basic commands.

In part 4, it has been optimized a resonant cavity for chemical application to obtain the desired field distribution on the samples placed inside the cavity in order to apply certain chemical reactions. The optimization system is similar to that presented in the previous part, but in this case CST microwave Studio has been used for the device simulation.

Finally, the part 5 describes the optimization of an AMC-EBG structure to realize particular structures usable as absorber or as substrate for antenna application. The optimization has been achieved with the same technique described in part 3.

Part I

Particle Swarm Optimization

The global optimization methods can be divided in deterministic (like the gradient-based algorithms) and stochastic methods. Most of the optimization techniques evaluates the derivatives of the function to individuate the optima in the searching space. This method results difficult when the first derivative evaluation is made complex by rough or discontinuous domains. Swarm intelligence is a term conied in 1989 by Beni [7] to describes the collective behaviour of self-organized systems, taking inspiration by the colonies of animals in nature, such as flocks of birds, schools of fishes or swarms of bees. The studies on the beaviour of these group of animals led to the definition of several algorithms for the solutions of complex problems, like Ant colony optimizations (ACO) or Particle Swarm optimization (PSO)

The PSO is an iterative algorithm developed by Kennedy and Eberhart in the 90s [8], [9] for continuous non-linear functions, designed to find out the solution of optimization problems, very efficient in solving multidimensional problems in a large variety of applications. As the other similar algorithms, it takes inspiration from the animal kingdom, in particular from the group movement in search of a common objective, as in a bees group: the movement of each individual is based on its own instinct, on the memory of its path and on the iterations with all other individuals.

It has many similarities with other evolutionary algorithm, like the most popular one, the Genetic Algorithm (GA). Both algorithms are inizialized with a random population, and both use a fitness function to assign a value to each individual of the population, and update it to reach the optimum solution with randomic processes. However, both don't guarantee a success. Basically, the PSO is based on the social movement whereas the GA is based on genetic enconding and fittest's selection. This detail requires that the particles of PSO have a memory, which is not present in the GAs: different from the genetic algorithms, the social behaviour of the individuals evolution is based on the "cooperation" with the other individuals instead of by means genetic operators. The main advantage of PSO respect to GA is its easier implementation: GA requires 3 main operations, that are selection, crossover and mutation, PSO has only a simple operation that is the velocity calculation. The particles update themselves through their velocity inside the solution space. Moreover, it doesn't require a conversion of the parameters to be optimize from real values to binary. The only

information the particles share each other is the coordinate of the best position reached by the particles in their evolution. PSO often converges to the optimal solution with fewer objective function evaluations than are required by GAs.

1 Classic PSO

First versions have been proposed in 1995[8] showing an optimization ability. In [9] different versions of the algorithm have been proposed, one model of global optimization and two for the local one. PSO optimizes a problem by having a population of candidate solutions and moving them around in the search-space according to simple mathematical formulae over the particle's position and velocity.

In the following, let's give a definition of the main keywords to understand how the algorithm works.

- Particle - An individual of the population. It represent a potential solution to a problem
- Solution space - It represents the set of admissible solutions and it's defined by the range in which to search for the optimal solution.This requires specifications of a maximum and minimum value for each dimension (N-dimensional optimization)
- Swarm - The group of particles which move inside the solution space
- Agent/Particle - An individual of the swarm, it moves iteratively according to general principles. It's described by the variables of the problem to be optimized (which constitute its coordinates in the solution space) and represents a solution of the problem.
- Position x - Each position inside the solution space represents a potential solution of the problem and it is described by a vector x. The vector x consists of the coordinates of the solution space where the particle is in that particular step.
- Fitness function f(x) - All swarm-intelligence algorithms need a method to evaluate the goodness of every position in the solution space. The fitness function associates a single number to each position in the solution space, establishing a link between the physical problem and the optimization algorithm.
- Personal best (p_{best}) - The position with the highest fitness value (best solution) encountered by the single agent along its path.
- Global best (g_{best}) - The location with the highest fitness value (best solution) encountered by the whole swarm.
- Velocity v - It determinates the direction in which the particle will move in the next iteration

The swarm is randomly initialized and its particles move iteratively inside a predetermined solution space, trying to reach the best position, defined by the best value of the fitness function associated to the optimization problem. Swarm position vary influenced by velocity: the particle of the swarm fly through the space leaded by the memory of their own best position and the knowledge oh the global best position. The algorithm proceeds iteratively, in the i-th iteration each particles is characterized by its position and velocity. Next position (1), direction and velocity (2) of each particle are updated according its position and velocity at the previous step, the p_{best} and the g_{best}. Considering a problem with p variables optimized by using q particles, for the i-th particle at the j-th step the next position is computed as

$$\mathbf{x}_{i,j} = \mathbf{x}_{i,j-1} + \mathbf{v}_{i,j} \tag{1}$$

As regards the velocity the first version has been presented in [9]

$$\mathbf{v}_{i,j} = \mathbf{v}_{i,j-1} + c_1 * \mathbf{r}_1 * (p_{best,i} - \mathbf{x}_{i,j-1}) + c_2 * \mathbf{r}_2 * (g_{best} - \mathbf{x}_{i,j-1}) \tag{2}$$

where $\mathbf{x}, \mathbf{v}, \mathbf{r}_1, \mathbf{r}_2 \in \mathbb{R}^{(q \times p)}$. Note that the matrices are multiplied element-by-element.

The presence of the first term determines the ability to explore the search space, this correction is effective for optimizing a wide range of functions: if the first term is removed, the algorithm can find a global minimum only when it's within the initial search space. r_1, r_2 are two random real numbers between 0.0 and 1.0 which simulate the random component of the swarm behaviour. The acceleration constant c_1, c_2 are respectively named "self-confidence" and "swarm confidence" and provide a weight between the pull of p_{best} and p_{best}. c_1 determines how much the velocity of the particle is influenced by his personal best, c_2 determines the influence of the whole swarm. Hence, c_1 encourages each particle to the research in the solution space around its personal best, c_2 pushes the exploration toward the global maximum: in general, low values allow particle to roam far from the target before being attracted to, whereas an high values provides a movement strongly oriented to the target.

Velocity consists of three contributes. The first (v) is the inertial component, its role is to keep the particle moving in the same direction it has in the previous step. The second term ($c_1 * \mathbf{r}_1 * (p_{best,i} - \mathbf{x}_{i,j-1})$) is the cognitive component, it makes the particle to tend to return to the area of the search space in which it has found is highest fitness value. The third term ($c_2 * \mathbf{r}_2 * (g_{best} - \mathbf{x}_{i,j-1})$) is the social component and causes the particles to move toward the best region found by the whole swarm.

The update of the personal and global best positions are described by the equations

$$p_{best,j} = \begin{cases} p_{best,j-1} & f(x_j) > f(p_{best,j-1}) \\ x_j & f(x_j) < f(p_{best,j-1}) \end{cases} \tag{3}$$

$$g_{best,j} = \min_{i=1...np} p_{best,i,j} \tag{4}$$

In general, velocity is applied to position updating for a time-step Δt which is set to 1 in this work. The algorithm main steps are:

1. Definition of the solution space
2. Definition of the size of the swarm
3. Initialization of swarm position inside the solution space and velocity
4. Systematic particles movement in the solution space. For each particle:
   - Objective function evaluation (g_{best}, p_{best} update)
   - Velocity update
   - Position update (swarm movement)
5. Iteration of point 2 until a convergence criterion is reached

It applies the concept of social interaction to problem solving and does not use the gradient of the problem being optimized, so it does not require the optimization problem to be differential, as it is required in some classic optimization methods. PSO has a very simple implementation compared to GA or other algorithms and it has been applied in several different fields.

PSO has several advantages: it has no overlapping or mutation calculation ad genetic algorithm. Only the best particle has to transmit its information to the rest of the swarm, and adopt real numbers. On the other hand this algorithm suffers the local optima.

2 Modifications to standard algorithm

2.1 Inertia weights

In order to establish ad additional trade-off between the global and the local search, a new parameter named inertia weight w has been introduced in [10]

$$\mathbf{v}_{i,j} = w * \mathbf{v}_{i,j-1} + c_1 * \mathbf{r}_1 * (p_{best,i} - \mathbf{x}_{i,j-1}) + c_2 * \mathbf{r}_2 * (g_{best} - \mathbf{x}_{i,j-1})$$

In particular, as regards the n-th component of velocity

$$v_n = w * v_{n,j-1} + c_1 * r_1 * (p_{best,n} - x_{n,j-1}) + c_2 * r_2 * (g_{best,n} - x_{n,j-1})$$

where x_n, $p_{best,n}$, $g_{best,n}$ are the n-th coordinate of the position, the personal best and the global best.

The first term of the velocity represents the inertial velocity of the particle: the inertia weight w controls the velocity component of the particle in the same direction of the previous step. It has a role in balancing between global search and local search: it adds a tendency to expand the search space, improving the ability to explore new areas and giving the particles a better global search ability. If $w << 1$ only a little component in preserved and rapid changes of direction are possible. On other side, if w is high and $c1, c2$ are low, the particle difficulty change their direction: this imply a large exploration of the space but a hard convergence to the best position (inertia weight): a large inertia weight favours the global search (exploration) while small inertia weight favours local search (exploitation). In [11] Shi and Eberhart showed how a linear decreasing inertia weight provides a quick convergence: named w_{min}, w_{min} the maximum and minimum valued assigned for w, and max_iter the maximum number of iterations of the algorithm, the inertia weight at the i-th step is

$$w = w_{max} - \frac{w_{max} - w_{min}}{max\_iter} * iter_i$$

Other kinds of decreasing inertia weight have been proposed, like an exponential decreasing weight by Li[12]

$$w = (w_{initial} - w_{end} - d_1)e^{\frac{1}{1 + d_2 \frac{iter_i}{max\_iter}}}$$

where d_1, d_2 are two factors introduced to control w, or non-linear solutions like the following proposed by Chongpeng[13]

$$w = w_{end} + (w_{start} - wend)\left(1 - \left(\frac{iter_i}{iter_max}\right)^{k1}\right)^{k2}$$

where $k1, k2 \in \mathbb{N}$. However, the Shi solution is the most used in typical applications.

2.2 Velocity clamping

The velocity clamping limits the maximum velocity of each particle. If the velocity is higher than a maximum allowed value, it is set to a maximum value $v_{max}(j)$ that represent the

maximum speed in the $j-th$ direction. Hence, the j-th component of the velocity of the i-th particle is defined as

$$v_{ij} = \begin{cases} v'_{ij}(t+1) & v_{ij}(t+1) < v_{max}(j) \\ v_{max}(j) & otherwise \end{cases}$$

where

$$v_{max,j} = \alpha(x_{max,j} - x_{min,j})$$

with $\alpha \in (0,1)$ and $x_{min,j}$, $x_{max,j}$ are the boundaries of the solution space in the j-th dimension. This allows to control the global exploration of the swarm. High values of v_{max} encourage global explorations, low one the local exploration.

2.3 Constriction factor

Another technique to balance exploration and exploitation to insure convergence of the PSO is the constriction factor K, proposed by Clerc (1999). A simplified formula of this PSO version is

$$\mathbf{v}_{i,j} = K\left[\mathbf{v}_{i,j-1} + c_1 * \mathbf{r}_1 * (p_{best,i} - \mathbf{x}_{i,j-1}) + c_2 * \mathbf{r}_2 * (g_{best} - \mathbf{x}_{i,j-1})\right]$$

with

$$K = \frac{2k}{\|2 - \phi - \sqrt{\phi(\phi-4)}\|}$$

with $\phi = c_1 r_1 + c_2 r_2$

2.4 Boundary conditions

Velocity clamping, inertia and constriction factors cannot always confine the particle inside the solution space. To solve this problem, different solutions have been adopted by the authors

- Absorbing walls : if a particle reaches the boundary in one dimension, the velocity in that dimension is reset (zero)
- Reflecting walls : the sign of the velocity in the dimension in which the particle has hit the boundary is changed
- Invisible walls: particles can fly with no restrictions, if they are outside the solution space they are not evaluated for fitness

2.5 Cauchy mutation

In general, PSO can't guarantee to find the global minimal value of a function, but sometimes it converges to a local minimum. Different variants of PSO have been proposed to overcome this problem and improve the performance. Some mutate the global best particle and some mutate the local best particle with different techniques to prevent the PSO for stagnation in local minima

The Cauchy mutation is one of the techniques introduced into PSO algorithm to overcome this problem, proposed by Wang. The principle is to mutate the global best particle, compare its fitness with its original one, and chose the best one. The mutated position is computed as

$$g_{Cauchy} = g(i) + W(i) * N(xmax, xmin)$$

where g is the original global best and N is a Cauchy distributed function. W is the Cauchy mutation operator and it's a weight vector

$$W(i) = \frac{\sum_{j=1}^{np} v_{ij}}{np}$$

3 PSO in Electromagnetics

PSO has been introduced in microwave research by Robinson and Rahmat Samii[15] in 2004. They proposed the design of a profiled corrugated horn antenna, and the used the PSO to modify the geometric characteristics to obtains the desired peak cross-polarization, beamwidth and return loss. Its effectiveness with performance similar to GAs, the simple implementation and the easy integration with the numerical techniques allowed a rapid spread in the scientific community.

It has been applied to different application like pattern synthesis of array antennas: in [16], a log periodic dipole arrays has been designed to optimize the performances in terms of mean directive gain of the antenna at the broadside direction, front-back ratio, mean SWR and bandwidth. The Rahmat-Samii's research on the flexibility of PSO covers a wide range of topics. In [17], Jin and Rahmat-Samii proposed an hybrid real-binary PSO applied to several devices as antenna arrays (a low SLL optimization in terms of element location in a non uniform antenna array, or in term of on/off state in a thinned array), planar radar absorbing material arrays (a minimum radar cross section optimization in terms of the material and thickness of each layer) and dual-band patch antennas, in [18] an optimization of rectangular and E-shaped patch antennas through an integration of the PSO with a FDTD analysis is presented. Other applications presented by Rahmat-Samii's group involve reflector antenna shaping and EBG structures. In [19], a three-feed single-offset reflector antenna for simultaneous reception from multiple satellites was designed. The shape of the reflection surface and the other antenna parameter such as the positions, orientations, and excitations of feeds, are optimized by means a parallel PSO. In [20] an EBG unit cell is optimized by determining the metal/dielectric state of each pixel, so that the EBG structure has a $\pi/2$ reflection phase at a desired frequency.

Several researchers proposed the application of the PSO to the design of different devices: wideband antennas, frequency selective surfaces, dielectric filters, microwave multilayer planar absorbers. The algorithm turns out to be very efficient as regards the optimization of the geometrical dimensions or the dielectric properties of the materials. In [23] a CPW-fed antenna with a complex geometric structure is optimized by modifying its geometrical parameters by evaluating the performance through an interface between Matlab and HFSS. In [24] the optimization of a FSS is developed by incorporating real and binary numbers in the same algorithm to describe and optimize the unit cell. In [25],[26] the PSO is used to optimize

multilayer devices. In [25] a dielectric filter consisting of 7 layers is optimized by optimized the permittivity (with only a dataset of 15 available permittivity values) and the thickness (continuously variable) of each layer. In [26] the optimization of a multilayer microwave absorber for a desired range of frequency and angles of incidence is presented.

4 PSO and electromagnetic analysis

As explained above, each set of values assumed by each particle during its flight represent a potential solution of the problem, that is, a configuration of the device to be optimized. The fitness computation requests a em analysis program connected ot the objective function. Basically, two kinds of em analysis have been used in this work: a numerical technique directly developed in the same informatic language of the optimization tool (that is, Matlab) or a link between the algorithm and a CAD full wave software.

In the first case, the electromagnetic analysis is implemented through a set of Matlab scripts which are called by the objective function of the algorithm: the variables of the PSO that describe the particle are the input of such functions. This set of functions build a discretization of the device, solve an eigenvalue problem and evaluate the performance. The results are combined in a proper fitness function to obtain a value that will guide the next iterations to the optimal configuration.

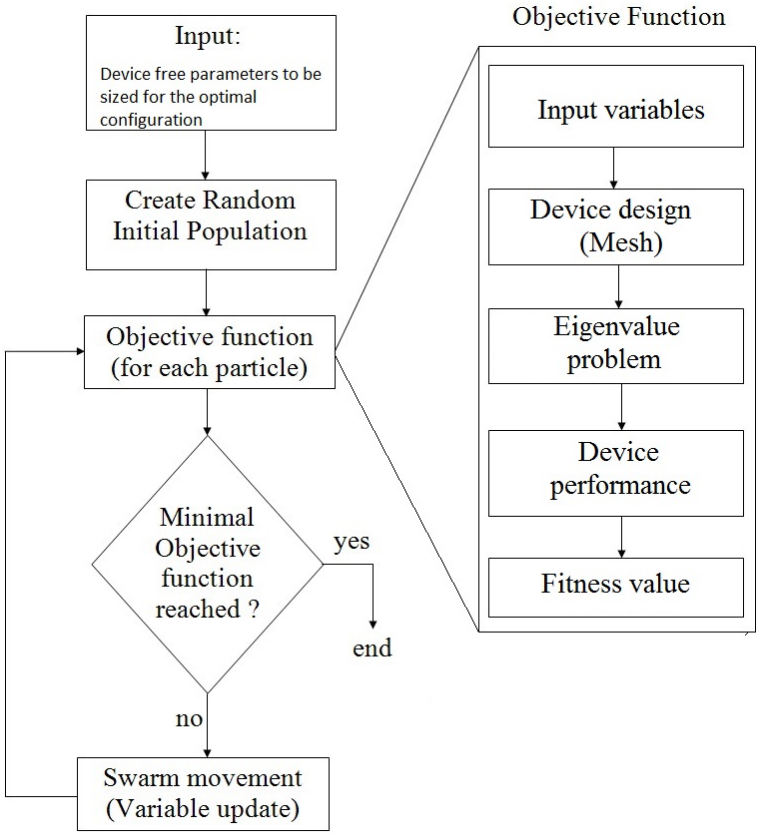

Figure 2: Optimization scheme : integration between PSO and electromagnetic analysis

The combined operation with a CAD requests the introduction of proper files that allow the exchange of information between the two softwares, as shown in figure 3. To do this, the objective function creates a Visual Basic script which send to the CAD (like CST or HFSS) the information obout the geometry of the device to be evaluated (that are, the variables to be optimized), the parameters of the simulation and which type results to be plotted. The CAD software run the simulation and send back to the objective function some text files which contains the results requested to compute the fitness.

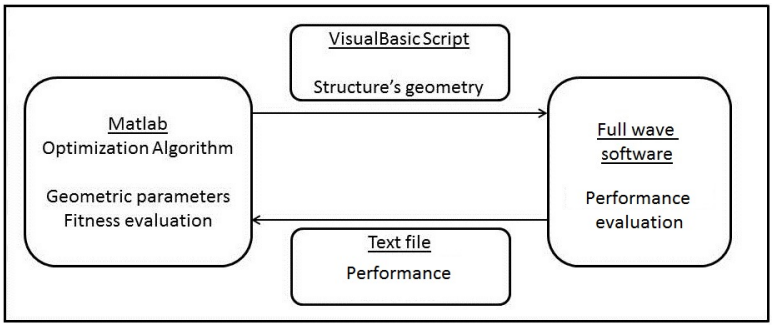

Figure 3: Combination of the optimization algorithm with a software for the simulation of electromagnetic fields

Part II

Ridge waveguide optimization

The propagation of intense microwave fields is required in several applications, ranging from radar to industrial heating. This propagation must be supported by a structure with low losses, high power handling capability (PHC) and able to confine the field to prevent compatibility problems. The most effective structures which fulfil these requests are the metallic hollow waveguides (WG). However, as it is well known, WG propagation displays a modal structure, and the propagation of each mode is high-pass and dispersive. WGs can be used only as long as sigle–mode propagation takes place, therefore, the useful bandwidth of a standard WG (rectangular or circular) is relatively narrow. Different WG shapes have therefore been proposed to increase the WG bandwidth. However, all of them affect negatively the PHC and the losses. So, the main goal is to increase the bandwidth without reducing too much the PHC and increasing the losses.

The most popular approach to increase significantly the bandwidth with a small negative effect on PHC and losses is the use of ridge waveguides (R-WG): since a suitable designed ridge WG has a smaller cut–off frequency f_0 of the fundamental mode, and a larger cut–off frequency f_1 of the first higher–order mode than a standard WG. The proposal of R-WGs dates back to the 40's, showing how rectangular R-WGs have a lower cutoff frequency and a greater dominant mode bandwidth compared to a standard rectangular WG with the same dimensions. However, in it is shown that a ridge structure provides a larger bandwidth but, on the other hand, it has a reduced power handling capability.

The opposite behaviour of bandwidth and PHC can limit the use of R-WGs. Moreover, the increase in the length of the boundary in R-WG can increase also the WG power losses. In order to get an effective trade-off between these conflicting requirements, a suitable optimization procedure should be devised, starting from an optimization algorithm able to explore, in an effective way, the solution space. However, the algorithm must work in tandem with an EM analysis program. Since the latter is the main determinant factor of the total computational time, its selection requires a careful evaluation. Though several numerical techniques exist for electromagnetic analysis of R-WGs, an effective in-house Finite-difference frequency-domain method (FDFD) has been realized to compute eigenvalues and mode distribution, whereas the optimization has been obtained by using the PSO algorithm. Different ridge WGs con-

figurations have been effectively optimized through a synergic use of PSO and the in-house FDFD, according to different requests of bandwidth, power handling and attenuation.

5 Finite-difference frequency-domain method

In microwave, the knowledge of the mode functions is useful in analysis of junction using mode matching or in the method of moment applied to to waveguide aperture. Both TE and TM modes in a guiding structure can be obtained from the solutions of the eigenvalue equation

$$\nabla_t^2 \phi + k_t^2 \phi = 0 \tag{5}$$

where ϕ is the scalar potential and k_t is the "transverse eigenvalue", from which the propagation constant and the characteristic impedance can be obtained. The different boundary condition applied on the conductive edge of the structure is different for the two types of modes

$$\frac{\partial \phi}{\partial n} = 0 \quad TE \tag{6}$$

$$\phi = 0 \quad TM \tag{7}$$

In general, the mode computation can't be done in closed form, so a numerical technique is

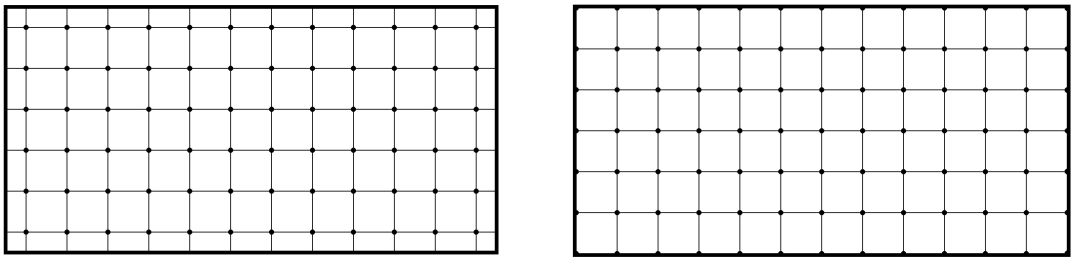

Figure 4: TE (left) and TM (right) grid for a rectangular waveguide

required. Such techniques require the definition of a grid of nodes where the analytic equation will be discretized, so the solution will be evaluated only on the nodes. Typically, the different boundary conditions lead to the definition of two different discretizations of the transverse section of the structure to evaluate separately TE and TM modes , as it can be seen in fig. 4 for a rectangular waveguide. Named Δx and Δy the discretization steps along the axes, the TE grid external nodes are $Dx/2$, $Dy/2$ distant from the conductor, whereas the TM nodes are Dx, Dy distant. This can cause some problems when the analysis involved the analysis of mode matching of discontinuities, so a model with only one grid would be preferred.

The Finite Difference Frequency Domain method (FDFD) is a numerical technique for the solution of differential equations, which requires a very simple formulation and have an high

computational effectiveness. It transforms Maxwell equations in the frequency domain or the Helmholtz equation in the matrix algebraic form

$$Ax = -k_t^2 x \tag{8}$$

whose eigenvectors x describe the potential discretized over the discretization points. The matrix A that represents the problem is sparse, this makes the computation very efficient. The finite difference approach is based on the replacement of the derivative with an its finite approximation, so, the solution is computed only on a finite sets of points, which are the nodes of the discretization grid.

By considering a single variable function $f(x)$, it can be approximated in the point x_0 by a Taylor Series expansion

$$f(x_0 + h) = f(x_0) + f'(x_0)h + \frac{f''(x_0)h}{2}h^2 + \cdots + \frac{f^{(n)}(x_0)h}{n!}h^n + R_n(x) \tag{9}$$

where $R_n(x_0)$ is the remainder term. An approximation for the first derivative is obtainable by truncating the Taylor approximation and dividing by h:

$$\frac{f(x_0 + h)}{h} = \frac{f(x_0)}{h} + f'(x_0) + \frac{R_n(x)}{h} \tag{10}$$

if $R_n(x)$ is small enough, it can be neglected and it is obtained the forward approximation for $f'(x)$ near the point x_0

$$f'(x_0) \cong \frac{f(x_0 + h) - f(x_0)}{h} \tag{11}$$

Similarly, the second derivative approximation can be obtained as

$$f''(x_0) \cong \frac{f(x_0 + h) - 2f(x_0) + f(x_0 - h)}{h^2} \tag{12}$$

The FD approach requests the substitution of the derivatives in (5), (6), (7) with a finite approximation. A simple application of the FDFD method consists on an approximation of the system at the second order in a Cartesian reference system for the mode evaluation in a rectangular waveguide. The eq. 5 in Cartesian coordinates

$$\frac{\partial^2 \phi}{\partial x^2} + \frac{\partial^2 \phi}{\partial y^2} = -k_t^2 \phi \tag{13}$$

must be discretized and approximated on a grid of point. In order to obtain a finite approximation of the partial derivatives in the generic point P, a representation of the potential in each node around P in terms of P itself is needed. Referring to fig (5), it follows

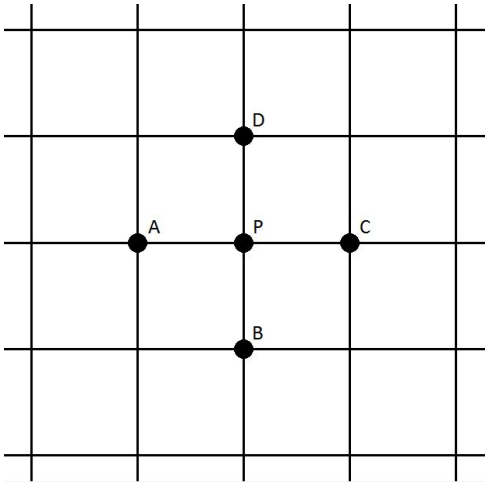

Figure 5: Discretization grid

$$\phi_A = \phi_P + \left.\frac{\partial\phi}{\partial x}\right|_P (-\Delta x) + \frac{1}{2}\left.\frac{\partial^2\phi}{\partial x^2}\right|_P (-\Delta x)^2 \tag{14}$$

$$\phi_B = \phi_P + \left.\frac{\partial\phi}{\partial x}\right|_P (-\Delta y) + \frac{1}{2}\left.\frac{\partial^2\phi}{\partial x^2}\right|_P (-\Delta y)^2 \tag{15}$$

$$\phi_C = \phi_P + \left.\frac{\partial\phi}{\partial x}\right|_P \Delta x + \frac{1}{2}\left.\frac{\partial^2\phi}{\partial x^2}\right|_P \Delta x^2 \tag{16}$$

$$\phi_D = \phi_P + \left.\frac{\partial\phi}{\partial x}\right|_P \Delta y + \frac{1}{2}\left.\frac{\partial^2\phi}{\partial x^2}\right|_P \Delta y^2 \tag{17}$$

Combining properly the Taylor approximations ((14) + (16) , (15) + (17)) a representation of (12) in terms of the grid nodes is obtained for x and y direction:

$$\frac{\partial^2\phi}{\partial x^2} \sim \frac{1}{\Delta x^2}(\phi_A + \phi_C - 2\phi_P) \tag{18}$$

$$\frac{\partial^2\phi}{\partial y^2} \sim \frac{1}{\Delta y^2}(\phi_B + \phi_D - 2\phi_P) \tag{19}$$

Therefore

$$\begin{aligned}\left.\nabla_t^2\phi\right|_P \sim \frac{1}{\Delta x^2}(\phi_A + \phi_C - 2\phi_P)\frac{1}{\Delta y^2}(\phi_B + \phi_D - 2\phi_P) = \\ = \frac{\phi_A}{\Delta x^2} + \frac{\phi_B}{\Delta y^2} + \frac{\phi_C}{\Delta x^2} + \frac{\phi_D}{\Delta y^2} - \left(\frac{2}{\Delta x^2} + \frac{2}{\Delta y^2}\right)\phi_P\end{aligned} \tag{20}$$

and the Helmholtz equation takes the form

$$\frac{\phi_A}{\Delta x^2} + \frac{\phi_B}{\Delta y^2} + \frac{\phi_C}{\Delta x^2} + \frac{\phi_D}{\Delta y^2} - 2\left(\frac{1}{\Delta x^2} + \frac{1}{\Delta y^2}\right)\phi_P = -k_c^2\phi_P \tag{21}$$

that is, by referring to a generic point in matricial terms

$$\frac{\phi_{i,j-1}}{\Delta x^2} + \frac{\phi_{i+1,j}}{\Delta y^2} + \frac{\phi_{i,j+1}}{\Delta x^2} + \frac{\phi_{i-1,j}}{\Delta y^2} - 2\left(\frac{1}{\Delta x^2} + \frac{1}{\Delta y^2}\right)\phi_{i,j} = -k_c^2\phi_{i,j} \tag{22}$$

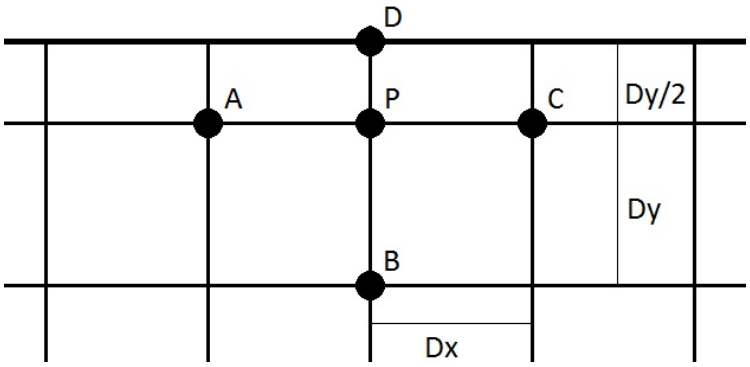

Figure 6: TE grid on the edge

The boundary points of the grids request another approach. By considering a TE mode, the potential in the generic point D on the edge, as in fig. (6), must verify the (6) and the expression (17) becomes

$$\phi_P = \phi_D - \left.\frac{\partial\phi}{\partial y}\right|_D \frac{\Delta y}{2} = \phi_D$$

and the (19)

$$\frac{\partial^2\phi}{\partial y^2} \sim \frac{1}{\Delta y^2}(\phi_B - \phi_P)$$

thus, the (20)

$$\left.\nabla_t^2\phi\right|_P \sim \frac{1}{\Delta x^2}(\phi_A + \phi_C - 2\phi_P) + \frac{1}{\Delta y^2}(\phi_B - \phi_P) = \\ = \frac{\phi_A}{\Delta x^2} + \frac{\phi_B}{\Delta y^2} + \frac{\phi_C}{\Delta x^2} - \left(\frac{2}{\Delta x^2} + \frac{1}{\Delta y^2}\right)\phi_P \quad (23)$$

The Helmholtz equation, in matricial terms, takes the form

$$\frac{\phi_{i,j-1}}{\Delta x^2} + \frac{\phi_{i-1,j}}{\Delta y^2} + \frac{\phi_{i,j+1}}{\Delta x^2} - \left(\frac{2}{\Delta x^2} + \frac{1}{\Delta y^2}\right)\phi_{i,j} = -k_c^2\phi_{i,j} \quad (24)$$

As regards a point on the corner it is

$$\left.\frac{\partial\phi}{\partial y}\right|_D = 0 \qquad \left.\frac{\partial\phi}{\partial x}\right|_C = 0$$

and

$$\phi_C = \phi_P \quad \Rightarrow \quad \frac{\partial^2\phi}{\partial x^2} \sim \frac{1}{\Delta x^2}(\phi_A - \phi_P)$$

$$\phi_D = \phi_P \quad \Rightarrow \quad \frac{\partial^2\phi}{\partial y^2} \sim \frac{1}{\Delta y^2}(\phi_B - \phi_P)$$

$$\left.\nabla_t^2\phi\right|_P \sim \frac{1}{\Delta x^2}(\phi_A - \phi_P) + \frac{1}{\Delta y^2}(\phi_B - \phi_P) = \frac{\phi_A}{\Delta x^2} + \frac{\phi_B}{\Delta y^2} - \left(\frac{1}{\Delta x^2} + \frac{1}{\Delta y^2}\right)\phi_P \quad (25)$$

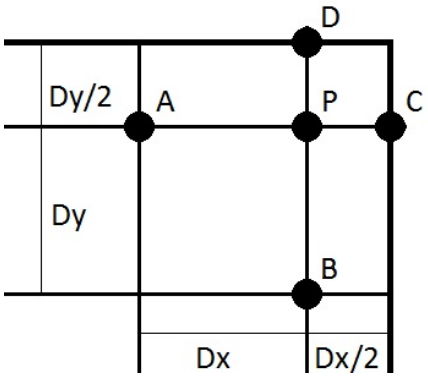

Figure 7: TE grid on a corner

thus, the 13 in matricial terms becomes

$$\frac{\phi_{i,j-1}}{\Delta x^2} + \frac{\phi_{i+1,j}}{\Delta y^2} - \left(\frac{1}{\Delta x^2} + \frac{1}{\Delta y^2}\right)\phi_{i,j} = -k_c^2\phi_{i,j} \tag{26}$$

Thus, the linear system which provide the potential on the transverse section consists on equations like

$$\frac{\phi_{i,j-1}}{\Delta x^2} + \frac{\phi_{i+1,j}}{\Delta y^2} + \frac{\phi_{i,j+1}}{\Delta x^2} + \frac{\phi_{i-1,j}}{\Delta y^2} - 2\left(\frac{1}{\Delta x^2} + \frac{1}{\Delta y^2}\right)\phi_{i,j} = -k_c^2\phi_{i,j} \tag{27}$$

$$\frac{\phi_{i,j-1}}{\Delta x^2} + \frac{\phi_{i-1,j}}{\Delta y^2} + \frac{\phi_{i,j+1}}{\Delta x^2} - \left(\frac{2}{\Delta x^2} + \frac{1}{\Delta y^2}\right)\phi_{i,j} = -k_c^2\phi_{i,j} \tag{28}$$

$$\frac{\phi_{i,j-1}}{\Delta x^2} + \frac{\phi_{i+1,j}}{\Delta y^2} - \left(\frac{1}{\Delta x^2} + \frac{1}{\Delta y^2}\right)\phi_{i,j} = -k_c^2\phi_{i,j} \tag{29}$$

This representation implies that each line of the A matrix contains at most five non-zero elements, so the system is sparse and the FDFD is very effective to achieve the solution.

5.1 Approximation of the fourth order

The traditional 2nd-order FDFD scheme can be extended to the 4th order to obtain a more precise description of the field distribution. A 4th order scheme provides an higher precision for the same discretization step compared to the 2nd order, thus, it allows to use a less dense grid to obtain the same precision. In this case, the A matrix is very smaller and slightly less sparse, so the computation time results to be reduced.

5.1.1 Cartesian case

Considering a regular Cartesian grid with step $(\Delta x, \Delta y)$ and defining the generic sample as $\phi_{i,j} = \phi(i\Delta x, j\Delta y)$, the equation can be discretized in the point P. Repeating the method

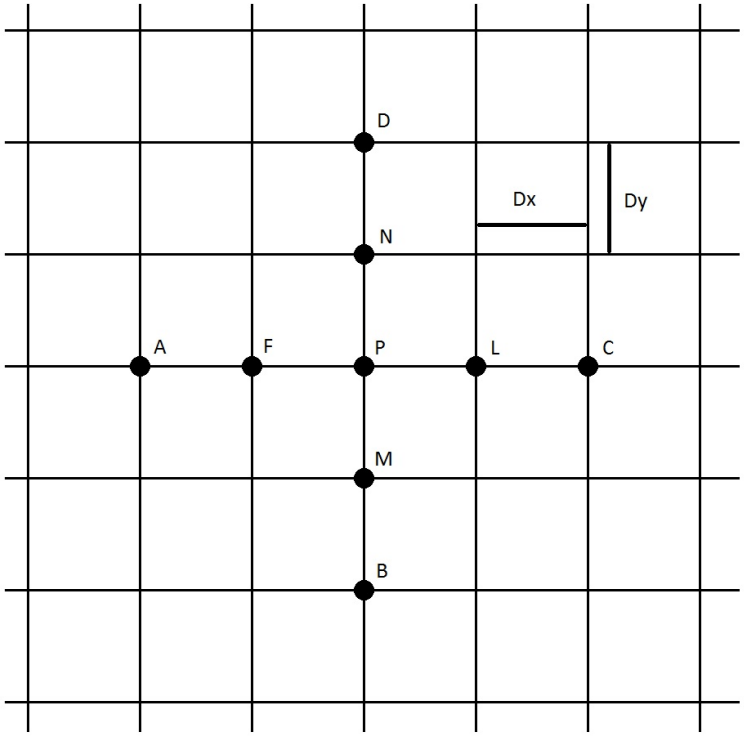

Figure 8: FDFD grid - internal point

applied in (14-17), the potential in each node referred to the reference point P . As regards the direction y, it follows

$$\phi_D = \phi_P + \left.\frac{\partial\phi}{\partial y}\right|_P (2\Delta y) + \frac{1}{2}\left.\frac{\partial^2\phi}{\partial y^2}\right|_P (2\Delta y)^2 + \frac{1}{6}\left.\frac{\partial^3\phi}{\partial y^3}\right|_P (2\Delta y)^3 + \frac{1}{24}\left.\frac{\partial^4\phi}{\partial y^4}\right|_P (2\Delta y)^4$$

$$\phi_N = \phi_P + \left.\frac{\partial\phi}{\partial y}\right|_P (\Delta y) + \frac{1}{2}\left.\frac{\partial^2\phi}{\partial y^2}\right|_P (\Delta y)^2 + \frac{1}{6}\left.\frac{\partial^3\phi}{\partial y^3}\right|_P (\Delta y)^3 + \frac{1}{24}\left.\frac{\partial^4\phi}{\partial y^4}\right|_P (\Delta y)^4$$

$$\phi_M = \phi_P + \left.\frac{\partial\phi}{\partial y}\right|_P (-\Delta y) + \frac{1}{2}\left.\frac{\partial^2\phi}{\partial y^2}\right|_P (-\Delta y)^2 + \frac{1}{6}\left.\frac{\partial^3\phi}{\partial y^3}\right|_P (-\Delta y)^3 + \frac{1}{24}\left.\frac{\partial^4\phi}{\partial y^4}\right|_P (-\Delta y)^4$$

$$\phi_B = \phi_P + \left.\frac{\partial\phi}{\partial y}\right|_P (-2\Delta y) + \frac{1}{2}\left.\frac{\partial^2\phi}{\partial y^2}\right|_P (-2\Delta y)^2 + \frac{1}{6}\left.\frac{\partial^3\phi}{\partial y^3}\right|_P (-2\Delta y)^3 + \frac{1}{24}\left.\frac{\partial^4\phi}{\partial y^4}\right|_P (-2\Delta y)^4$$

In this case, the Taylor approximations results analytically complex, it has preferred to impose a finite terms expansion of the first term of the eigenvalue equation (5). This representation requires a less analytic complexity, and it's easily to generalize to other structures.

$$\left.\frac{\partial^2\phi}{\partial y^2}\right|_P \sim \sum_{i=D,N,M,B} A_i(\phi_i - \phi_P) =$$

$$A_D\phi_D + A_N\phi_N + A_M\phi_M + A_B\phi_B - (A_D + A_N + A_M + A_B)\phi_P \quad (30)$$

We impose that this expression is equal to

$$\left.\frac{\partial^2\phi}{\partial y^2}\right|_P = B_1\left.\frac{\partial\phi}{\partial y}\right|_P + B_2\left.\frac{\partial^2\phi}{\partial y^2}\right|_P + B_3\left.\frac{\partial^3\phi}{\partial y^3}\right|_P + B_4\left.\frac{\partial^4\phi}{\partial y^4}\right|_P$$

with the conditions

$$B_1 = 0 \qquad B_2 = 1 \qquad B_3 = 0 \qquad B_4 = 0$$

The equivalence leads to the matricial system

$$\begin{vmatrix} 2\Delta_y & \Delta y & -\Delta y & -2\Delta_y \\ \frac{(2\Delta y)^2}{2} & \frac{\Delta y^2}{2} & \frac{(-\Delta y)^2}{2} & \frac{(2\Delta y)^2}{2} \\ \frac{(2\Delta y)^3}{6} & \frac{\Delta y^3}{6} & \frac{(-\Delta y)^3}{6} & \frac{(2\Delta y)^3}{6} \\ \frac{(2\Delta y)^4}{24} & \frac{\Delta y^4}{24} & \frac{(-\Delta y)^4}{24} & \frac{(2\Delta y)^4}{24} \end{vmatrix} \begin{vmatrix} A_D \\ A_N \\ A_M \\ A_B \end{vmatrix} = \begin{vmatrix} B_1 \\ B_2 \\ B_3 \\ B_4 \end{vmatrix} \tag{31}$$

Such a system provides the values of the A_i coefficients, now it is possible to express the (30) as

$$\left.\frac{\partial^2\phi}{\partial y^2}\right|_P \sim -\frac{1}{12Dy^2}\phi_D - \frac{1}{12Dy^2}\phi_B + \frac{16}{12Dy^2}\phi_N + \frac{16}{12Dy^2}\phi_M - \frac{30}{12Dy^2}\phi_P \tag{32}$$

Similarly, in the x direction

$$\left.\frac{\partial^2\phi}{\partial x^2}\right|_P \sim -\frac{1}{12Dx^2}\phi_C - \frac{1}{12Dx^2}\phi_A + \frac{16}{12Dx^2}\phi_L + \frac{16}{12Dx^2}\phi_F - \frac{30}{12Dx^2}\phi_P \tag{33}$$

Therefore it is obtained:

$$\begin{aligned}\nabla_t^2\phi_P = \frac{1}{12}\left(-\frac{\phi_D}{Dy^2} - \frac{\phi_B}{Dy^2} + 16\frac{\phi_N}{Dy^2} + 16\frac{\phi_M}{Dy^2}\right) + \\ \frac{1}{12}\left(-\frac{\phi_C}{Dx^2} - \frac{\phi_A}{Dx^2} + 16\frac{\phi_L}{Dx^2} + 16\frac{\phi_F}{Dx^2}\right) + \\ -\frac{2}{12}\left(\frac{15}{Dy^2} + \frac{15}{Dx^2}\right)\phi_P\end{aligned} \tag{34}$$

This equation can be applied to all internal point in the grid to get the discretized form of Helmholtz

$$\begin{aligned}\frac{1}{12}\left(-\frac{\phi_{i+2,j}}{Dy^2} - \frac{\phi_{i-2,j}}{Dy^2} + 16\frac{\phi_{i+1,j}}{Dy^2} + 16\frac{\phi_{i-1,j}}{Dy^2}\right) + \\ \frac{1}{12}\left(-\frac{\phi_{i,j+2}}{Dy^2} - \frac{\phi_{i,j-2}}{Dy^2} + 16\frac{\phi_{i,j+1}}{Dy^2} + 16\frac{\phi_{i,j-1}}{Dy^2}\right) + \\ -\frac{2}{12}\left(\frac{15}{Dy^2} + \frac{15}{Dx^2}\right)\phi_{i,j} = -k_t^2\phi_{i,j}\end{aligned} \tag{35}$$

Equation (35) cannot be used for boundary points. As regards a point on the edge, it is

$$\left.\frac{\partial^2\phi}{\partial y^2}\right|_P \sim \sum_{i=B,M,S} A_i(\phi_i - \phi_P) = A_B\phi_B + A_M\phi_M + A_S\phi_S - (A_B + A_M + A_S)\phi_P$$

The analysis is different for TE and TM potentials evaluation.

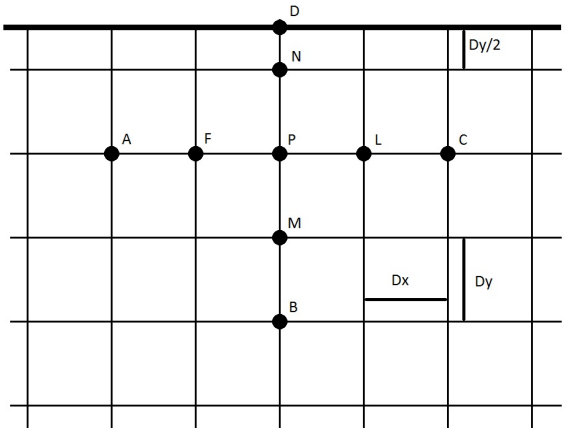

Figure 9: Boundary point for TE grid

As regards to the TE modes, referring to figure (9) and imposing the (6), it is

$$\left.\frac{\partial\phi}{\partial y}\right|_D \sim \left.\frac{\partial\phi}{\partial y}\right|_P + \left.\frac{\partial^2\phi}{\partial y^2}\right|_P \frac{\Delta y}{2} + \frac{1}{2}\left.\frac{\partial^3\phi}{\partial y^3}\right|_P \left(\frac{\Delta y}{2}\right)^2 + \frac{1}{6}\left.\frac{\partial^4\phi}{\partial y^4}\right|_P \left(\frac{\Delta y}{2}\right)^3 = 0$$

thus

$$\left.\frac{\partial\phi}{\partial y}\right|_P = -\left.\frac{\partial^2\phi}{\partial y^2}\right|_P \frac{\Delta y}{2} - \frac{1}{2}\left.\frac{\partial^3\phi}{\partial y^3}\right|_P \left(\frac{\Delta y}{2}\right)^2 - \frac{1}{6}\left.\frac{\partial^4\phi}{\partial y^4}\right|_P \left(\frac{\Delta y}{2}\right)^3 \tag{36}$$

By imposing a form like

$$\left.\frac{\partial^2\phi}{\partial y^2}\right|_P = B_1\left.\frac{\partial\phi}{\partial y}\right|_P + B_2\left.\frac{\partial^2\phi}{\partial y^2}\right|_P + B_3\left.\frac{\partial^3\phi}{\partial y^3}\right|_P + B_4\left.\frac{\partial^4\phi}{\partial y^4}\right|_P \tag{37}$$

and substituting (36) in (37)

$$\left.\frac{\partial^2\phi}{\partial y^2}\right|_P = \left[B_2 - B_1\frac{\Delta y}{2}\right]\left.\frac{\partial^2\phi}{\partial y^2}\right|_P + \left[B_3 - B_1\frac{1}{2}\left(\frac{\Delta y}{2}\right)^2\right]\left.\frac{\partial^3\phi}{\partial y^3}\right|_P + \left[B_4 - B_1\frac{1}{6}\left(\frac{\Delta y}{2}\right)^3\right]\left.\frac{\partial^4\phi}{\partial y^4}\right|_P \tag{38}$$

This equivalence in (38) is verified if

$$B_2 - B_1\frac{\Delta y}{2} = 1$$

$$B_3 - B_1\frac{1}{2}\left(\frac{\Delta y}{2}\right)^2 = 0$$

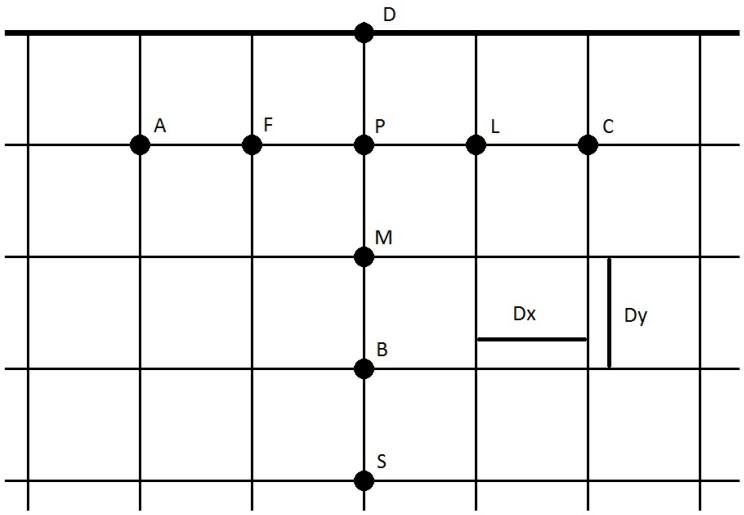

Figure 10: Boundary point for TM grid (1)

$$B_4 - B_1 \frac{1}{6}\left(\frac{\Delta y}{2}\right)^3 = 0$$

Applying a linear system as in the "normal" case, we found

$$\left.\frac{\partial^2\phi}{\partial y^2}\right|_P = \frac{1}{24\Delta v^2}\left(21\phi_M + 3\phi_B - \phi_S - 23\phi_P\right) \tag{39}$$

Adding (39) to (33) the finite approximation of (5) is obtained for a boundary point in the TE case

$$\nabla_T^2\phi = \left[\frac{\partial^2\phi}{\partial u^2} + \frac{\partial^2\phi}{\partial v^2}\right]_P =$$

$$= \frac{32}{24\Delta u^2}\phi_F + \frac{32}{24\Delta u^2}\phi_L - \frac{2}{24\Delta u^2}\phi_A - \frac{2}{24\Delta u^2}\phi_C + \frac{21}{24\Delta v^2}\phi_M + \frac{3}{24\Delta v^2}\phi_B - \frac{1}{24\Delta v^2}\phi_S$$
$$- \frac{1}{24}\left(\frac{60}{\Delta u^2} + \frac{23}{\Delta v^2}\right)\phi_P \tag{40}$$

As regards the TM mode, referring to fig. (10), since

$$\phi_D = 0$$

we have

$$\left.\frac{\partial^2\phi}{\partial v^2}\right|_P \sim \sum_{i=D,B,M,S} A_i\left(\phi_i - \phi_P\right) = A_B\phi_B + A_M\phi_M + A_S\phi_S - \left(A_B + A_D + A_M + A_S\right)\phi_P$$

Repeating the steps of the TE case, we obtain

$$\left.\frac{\partial^2\phi}{\partial y^2}\right|_P = \frac{7}{3\Delta v^2}\phi_M - \frac{2}{5\Delta v^2}\phi_B + \frac{1}{21\Delta v^2}\phi_S - \frac{16}{3\Delta v^2}\phi_P$$

that, added to (33), is

$$\left[\frac{\partial^2\phi}{\partial x^2}+\frac{\partial^2\phi}{\partial y^2}\right]_P = \frac{16}{12\Delta x^2}\phi_F + \frac{16}{12\Delta x^2}\phi_L - \frac{1}{12\Delta x^2}\phi_A - \frac{1}{12\Delta x^2}\phi_C + \frac{7}{3\Delta y^2}\phi_M - \frac{2}{5\Delta y^2}\phi_B +$$
$$+\frac{2}{21\Delta y^2}\phi_S - \left(\frac{30}{12\Delta x^2}+\frac{16}{3\Delta y^2}\right)\phi_P$$

As regards the point M, considering the points T,S,B and P

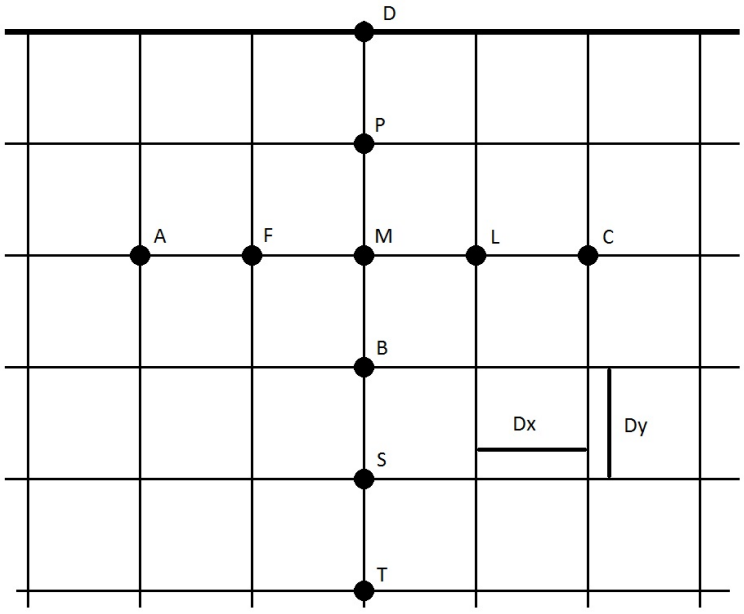

Figure 11: Boundary point for TM grid (2)

$$\left.\frac{\partial^2\phi}{\partial v^2}\right|_M = \frac{1}{12\Delta v^2}\left(11\phi_P + 6\phi_B + 4\phi_S - \phi_T - 20\phi_M\right)$$

the Laplace operator becomes

$$\left[\frac{\partial^2\phi}{\partial x^2}+\frac{\partial^2\phi}{\partial y^2}\right]_M = \frac{16}{12\Delta x^2}\phi_F + \frac{16}{12\Delta x^2}\phi_L - \frac{1}{12\Delta x^2}\phi_A - \frac{1}{12\Delta x^2}\phi_C + \frac{11}{12\Delta y^2}\phi_P + ...$$
$$+\frac{6}{12\Delta y^2}\phi_B + \frac{4}{12\Delta y^2}\phi_S - \frac{1}{12\Delta y^2}\phi_T - \frac{1}{12}\left(\frac{30}{\Delta x^2}+\frac{20}{\Delta y^2}\right)\phi_M$$

5.1.2 Elliptic case

A rectangular lattice of sampling points is a very accurate grid for rectangular and staircase ridges, whereas it reduces a curvilinear geometry to a staircase approximate structure. A suitable elliptical grid perfectly fits the boundary of a circular or elliptical waveguide, and it allows to evaluate the electromagnetic modes in an elliptical waveguide with the required

accuracy using order of magnitude less sampling points than the standard approach of FDFD, namely the use of a rectangular grid with a staircase approximation of the boundary.

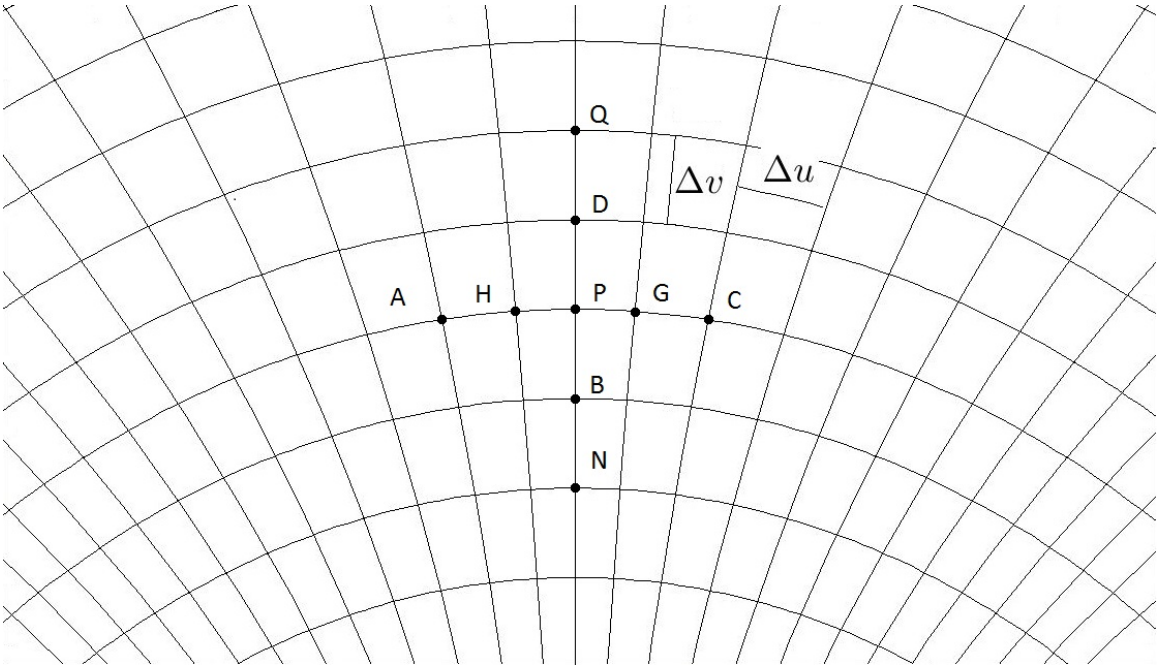

Figure 12: Elliptic grid

Similarly to Cartesian case, the figure (12) shows the scheme of sampling points to be considered in the elliptic coordinates applications of the FD approximation. The second derivative along the u-axis, involves the approximation of ϕ in the points Q, D, B, N referred to P

$$\phi_B = \phi_P + \left.\frac{\partial\phi}{\partial u}\right|_P(-\Delta u) + \frac{1}{2}\left.\frac{\partial^2\phi}{\partial u^2}\right|_P(-\Delta u)^2 + \frac{1}{6}\left.\frac{\partial^3\phi}{\partial u^3}\right|_P(-\Delta u)^3 + \frac{1}{24}\left.\frac{\partial^4\phi}{\partial u^4}\right|_P(-\Delta u)^4 \quad (41)$$

$$\phi_N = \phi_P + \left.\frac{\partial\phi}{\partial u}\right|_P(-2\Delta u) + \frac{1}{2}\left.\frac{\partial^2\phi}{\partial u^2}\right|_P(-2\Delta u)^2 + \frac{1}{6}\left.\frac{\partial^3\phi}{\partial u^3}\right|_P(-2\Delta u)^3 + \frac{1}{24}\left.\frac{\partial^4\phi}{\partial u^4}\right|_P(-2\Delta u)^4 \quad (42)$$

$$\phi_D = \phi_P + \left.\frac{\partial\phi}{\partial u}\right|_P(\Delta u) + \frac{1}{2}\left.\frac{\partial^2\phi}{\partial u^2}\right|_P(\Delta u)^2 + \frac{1}{6}\left.\frac{\partial^3\phi}{\partial u^3}\right|_P(\Delta u)^3 + \frac{1}{24}\left.\frac{\partial^4\phi}{\partial u^4}\right|_P(\Delta u)^4 \quad (43)$$

$$\phi_Q = \phi_P + \left.\frac{\partial\phi}{\partial u}\right|_P(2\Delta u) + \frac{1}{2}\left.\frac{\partial^2\phi}{\partial u^2}\right|_P(2\Delta u)^2 + \frac{1}{6}\left.\frac{\partial^3\phi}{\partial u^3}\right|_P(2\Delta u)^3 + \frac{1}{24}\left.\frac{\partial^4\phi}{\partial u^4}\right|_P(2\Delta u)^4 \quad (44)$$

leading to

$$\left.\frac{\partial^2\phi}{\partial u^2}\right|_P = \frac{1}{12}\frac{1}{\Delta u^2}\left(16\phi_B + 16\phi_D - \phi_N - \phi_Q - 30\phi_P\right) \quad (45)$$

Analogously, in the v direction

$$\left.\frac{\partial^2\phi}{\partial v^2}\right|_P = \frac{1}{12}\frac{1}{\Delta v^2}\left(16\phi_H + 16\phi_G - \phi_A - \phi_C - 30\phi_P\right) \quad (46)$$

Thus we have a discrete approximation of the nabla operator which provide a formulation of the Helmholtz equation suitable for the FDFD

$$\nabla_t^2\phi = \frac{\partial^2\phi}{\partial u^2} + \frac{\partial^2\phi}{\partial v^2} =$$
$$\frac{16}{12\nabla v^2}\phi_H + \frac{16}{12\nabla v^2}\phi_G - \frac{1}{12\nabla v^2}\phi_A - \frac{1}{12\nabla v^2}\phi_C \frac{16}{12\nabla u^2}\phi_B + \frac{16}{12\nabla u^2}\phi_D - \frac{1}{12\nabla u^2}\phi_N - \frac{1}{12\nabla u^2}\phi_Q +$$
$$- \frac{30}{12}\left(\frac{1}{\Delta u^2} + \frac{1}{\Delta v^2}\right)\phi_P \quad (47)$$

Because of singularities problem, this formulation is not applicable in the foci of the ellipse and in its major axis.

For a point P lying on the segment joining the two foci, it is $u = 0$. Therefore, P is a singular point of the grid, but the potential must be regular. To solve the equation in this points, the Helmholtz equation is integrated in the cell S_F , of sizes $\Delta x \times \Delta y$ centered in P, as

$$\int_{S_F} \nabla_t^2\phi dS = -k_t^2 \int_{S_F} \phi dS$$

and through the Gauss theorem it becomes a problem of the border Γ_F of the cell around the point

$$\int_{\Gamma_F} \frac{\partial\phi}{\partial n} \cdot dl = -k_t^2 \int_{S_F} \phi dS$$

then, the second term can be substituted with the value ϕ_X of the potential in the center X of the discretization cell S_F.

$$\int_{\Gamma_F} \frac{\partial\phi}{\partial n} \cdot dl = -k_t^2 \phi_X \hat{S}$$

where $\hat{S}$ is the cell area. So the equation to be considered in the eigenvalue problem is

$$\frac{1}{\hat{S}} \int_{\Gamma_F} \frac{\partial\phi}{\partial n} \cdot dl = -k_t^2 \phi_X$$

To evaluate the left hand side, Γ_F is divided into (curved) segments, along the coordinate curves, and the normal derivative is evaluated in finite terms. The first term of this equation is dicretized by evaluating the derivative over four points around the focus along each axis, following the same method described for the internal points.

As regards the boundary point, it is possible to distinguish between two cases: a "radial" and an "angular" case. For the first case (see fig. (13) on the left)

$$\left.\frac{\partial^2\phi}{\partial u^2}\right|_P \sim \sum_{i=B,N,S} F_i(\phi_i - \phi_P) = \left[T_1 \left.\frac{\partial\phi}{\partial u}\right|_P + T_2 \left.\frac{\partial^2\phi}{\partial u^2}\right|_P + T_3 \left.\frac{\partial^2\phi}{\partial u^3}\right|_P + T_4 \left.\frac{\partial^2\phi}{\partial u^4}\right|_P\right] \quad (48)$$

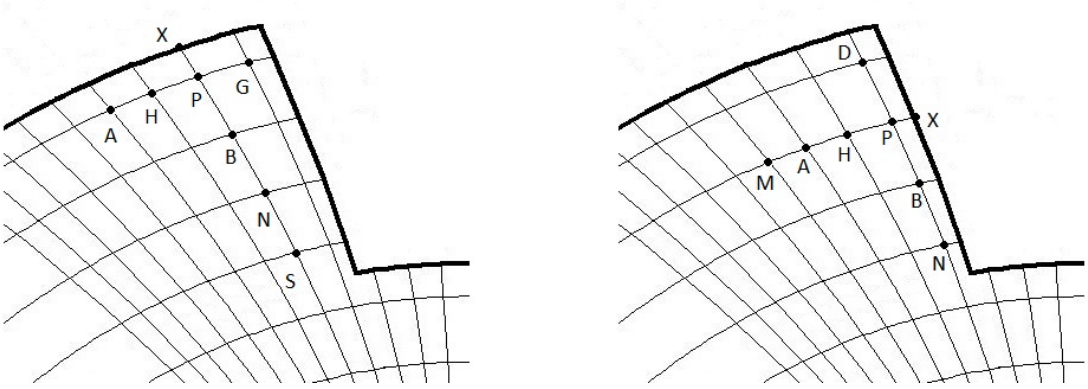

Figure 13: Boundary points on elliptic ridge

where the T_k are linear combination of the unknown F_i coefficient

$$T_k = \sum_{i=B,N,S} F_i \cdot \Delta u_i^k \tag{49}$$

As regards the TE boundary condition, we can expand it as

$$\left.\frac{\partial\phi}{\partial u}\right|_x \cong \left.\frac{\partial\phi}{\partial u}\right|_P + \left.\frac{\partial^2\phi}{\partial u^2}\right|_P \left(\frac{\Delta u}{2}\right) + \frac{1}{2}\left.\frac{\partial^3\phi}{\partial u^3}\right|_P \left(\frac{\Delta u}{2}\right)^2 + \frac{1}{6}\left.\frac{\partial^4\phi}{\partial u^4}\right|_P \left(\frac{\Delta u}{2}\right)^3 = 0 \tag{50}$$

and, spelling out $\left.\frac{\partial\phi}{\partial u}\right|_P$ from (50) and substituting in the right side of (48)

$$\left(T_2 - T_1\frac{\Delta u}{2}\right)\cdot\left.\frac{\partial^2\phi}{\partial u^2}\right|_P + \left(T_3 - T_1\frac{\Delta u^2}{8}\right)\cdot\left.\frac{\partial^3\phi}{\partial u^3}\right|_P + \left(T_4 - T_1\frac{\Delta u^3}{48}\right)\cdot\left.\frac{\partial^4\phi}{\partial u^4}\right|_P \tag{51}$$

This is an approximation of $\left.\frac{\partial^2\phi}{\partial u^2}\right|_P$ if

$$\begin{cases} T_2 - T_1\dfrac{\Delta u}{2} = 1 \\ T_3 - T_1\dfrac{\Delta u^2}{8} = 0 \\ T_4 - T_1\dfrac{\Delta u^3}{48} = 0 \end{cases} \tag{52}$$

And the F_i are obtained from the linear system 52. So, the (45) becomes

$$\left.\frac{\partial^2\phi}{\partial u^2}\right|_P = \frac{1}{24\Delta u^2}\left(21\phi_B + 3\phi_N - \phi_S - 23\phi_P\right) \tag{53}$$

and the Helmholtz equation has the shape

$$\frac{21}{24\Delta u^2}\phi_B + \frac{3}{24\Delta u^2}\phi_N - \frac{1}{24\Delta u^2}\phi_S + \frac{1}{\Delta v^2}\phi_H + \frac{1}{\Delta v^2}\phi_G - \left(\frac{23}{24\Delta u^2} + \frac{2}{\Delta v^2}\right)\phi_P \cong -k_t^2\phi_P^2 \tag{54}$$

The TM modes can be computed with the same TE grid, by imposing the BC $\phi_X = 0$ and expressing the potential in X through a Taylor approximations

$$\phi_X = \phi_P + \left.\frac{\partial\phi}{\partial u}\right|_P \left(\frac{\Delta u}{2}\right) + \frac{1}{2}\left.\frac{\partial^2\phi}{\partial u^2}\right|_P \left(\frac{\Delta u}{2}\right)^2 + \frac{1}{6}\left.\frac{\partial^3\phi}{\partial u^3}\right|_P \left(\frac{\Delta u}{2}\right)^3 + \frac{1}{24}\left.\frac{\partial^4\phi}{\partial u^4}\right|_P \left(\frac{\Delta u}{2}\right)^4 = 0 \quad (55)$$

Extracting $\left.\frac{\partial^2\phi}{\partial u^2}\right|_P$ from (55) and substituting it in (48), and solving the linear system (51), it is found the expression for the second derivative in P

$$\left.\frac{\partial^2\phi}{\partial u^2}\right|_P = \frac{7}{3\Delta u^2}\phi_B - \frac{2}{5\Delta u^2}\phi_N + \frac{1}{12\Delta u^2}\phi_S - \frac{16}{3\Delta u^2}\phi_P \quad (56)$$

Substituting (46) and (56) in (47) we have the final expression for the Helmholtz equation in the edge point

$$\frac{7}{3\Delta u^2}\phi_B - \frac{2}{5\Delta u^2}\phi_N + \frac{1}{21\Delta u^2}\phi_S - \frac{1}{3\Delta v^2}\phi_G + \frac{5}{3\Delta v^2}\phi_H - \frac{2}{15\Delta v^2}\phi_A + \left(\frac{4}{\delta v^2} + \frac{16}{3\Delta u^2}\right)\phi_P \cong -k_t^2\phi_P^2 \quad (57)$$

All other points can be dealt with in the same way as for TE modes.

6 Techniques of field computation

The first approach to the electromagnetic analysis of rectangular R-WG [27], [28] is the transverse resonance technique (TRT) [29]. TRT is able to compute, in an approximate way, the cut-off frequencies of the first few modes of a R-WG and their attenuation. Moreover, Hopfer[28] was able to compute also the power handling capability (PHC) taking also into account, in an approximate way, the singular behaviour of the field at the edges of ridges. Of course, numerical techniques such as FDFD[31] or FEM[32] allows to compute cut-off frequencies and modal distribution of a R-WG with a far better accuracy. The FDFD approach is the simplest numerical strategy to compute eigenvalues and modes of metallic hollow WGs and therefore it is well tailored to be used in PSO but it is useful also in procedure based on method of moments (MoM) or mode-matching (MM). The WG section is partitioned in a set of

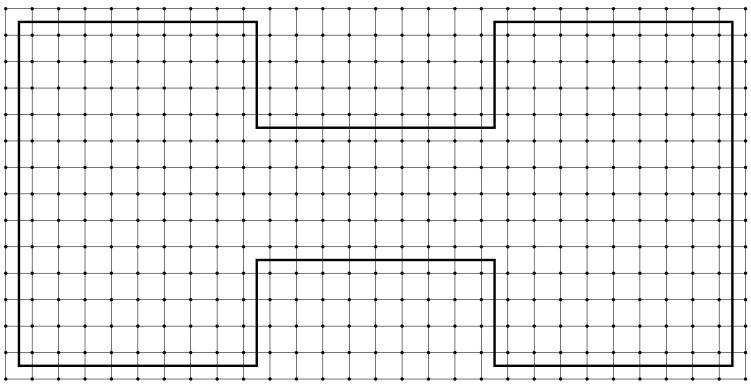

Figure 14: TE grid for FDFD analysis of ridge waveguides

regular discretization cells (fig. 14), and the differential eigenvalue problem represented by the Helmholtz equation is replaced by a finite difference one, using suitable Taylor approximations of second or fourth order. The standard FDFD approach, using two Cartesian sampling grids (one for TE modes and the other for TM, due to the different boundary conditions), allows a very effective solution for rectangular waveguides or, more generally, for WG with piecewise rectangular boundaries, since in these cases the boundary is perfectly fitted to the discretization grid, either uniform or non-uniform. The FDFD has been suitably generalized to evaluate all modes (either TE or TM) on a single grid. The discretization results in a matrix eigenvalue problem, which is sparse, so a very effective computation is possible. Once the eigenvalue problem is solved, the smallest two eigenvalues gives directly the WG bandwidth. The approach has been generalized to reach a comparable accuracy and computational load for

other geometries, including trapezoidal ones, which is of interest in R-WG analysis. Moreover, the devised approach is able to evaluate both TE and TM modes on the same grid.

Once the eigenvalue problem is solved, the smallest two eigenvalues gives directly the WG bandwidth. The respective eigenvectors represent the potential distribution of the first two modes. From the potential, it's easy to obtain the field distribution. The knowledge of the field distribution allows to compute the power flux P through a transverse section of a R-WG using its relationship with the total energy for unit length WEM [28].

7 Power evaluation

The PHC depends on both the WG shape and, for hollow WGs, the dielectric capability of the air. In order to compare different R-WGs, the maximum value of $|E|$ has been set to 1.

Two different ways have been investigated to evaluate the power.

The first technique had been proposed by Hopfer [28], who started its study from the relation between the power flux P and the total energy for unit length W_{EM}

$$P = W_{EM} \frac{k_z c}{k_0}$$

Basically, the TRT proposed by Hopfer evaluates the power by considering the field constant along the short side of the waveguide (which is true for a rectangular WG but not for a ridged one) and adding the capacitance contribution at the edge of the ridges. It defines an analytic representation of V of the first mode along the long side following the transmission line theory, that results in a sinusoidal function. The V is described by different functions in different areas of the WG, and boundary and symmetry conditions are exploited to obtain the formula. The square of these functions are integrated over the area of the trasverse section of the WG. Hopher computed the approximated analytic expression for the power carried by the ridged waveguide with a single o double ridge centered along the long side. For a double ridge waveguide (fig. 15), with the ridges centered along the long sides, the PHC can be computed as

$$P = \frac{1}{\sqrt{\epsilon_0 \mu_0}} \frac{\lambda_0}{\lambda_g} \left[2 \left(\frac{1}{2} C V_0^2 \right) + \frac{\epsilon_0}{2} \int_S E^2 dS \right]$$

where $E = bV$ (or dV in the area where there are the ridges, with d height of the guide in the ridged area) and $1/2CV^2$ is the contribute of the fringing field on the edge of the ridge. C is the capacitance equivalent to each height discontinuity and it is evaluated through the approximate formula

$$C = \frac{2\epsilon_0}{\pi} ln \left[csc \left(\frac{\pi d}{2b} \right) \right]$$

and V_0 is the fundamental mode voltage at the ridge edge.

Despite of the reduced accuracy, the TRT used by Hopfer is still a useful tool for the "back-to-envelope" evaluation of the cut-off frequency of the fundamental mode[30]. Despite the accuracy is not comparable with the nunerical techniques, the TRT is sufficient to compute the PHC of a R-WG. The total energy can be evaluated on the transmission-line equivalent circuit used for TRT. In [5] the six-ridges case has been described (Fig. 17 represents the TLM of only half of the transversal section of a six-ridge WG, so it stores half of the total energy),

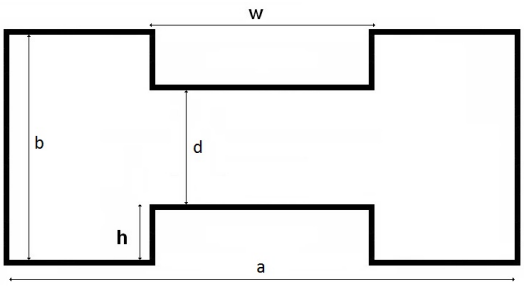

Figure 15: Double ridge waveguide

which requires some additional considerations respect to the double-ridge case described in[28]. The TRT starts by considering the transversal section of the R-WG as a resonator. The propagation constant is the same for each line (representing a parallel plate section of the R-WG) and it is equal to the transverse propagation constant kt, while the impedance is proportional to the WG height. To evaluate the PHC, a voltage VM corresponding to the maximum electric field is set at the open-circuit (i.e., at the WG center), and an unknown current IS at the short circuit end (i.e. at the WG lateral wall).

The total energy can be evaluated on the transmission-line equivalent circuit used for TRT. Since the double-ridge case is discussed in an appendix of [28], in this work the six-ridges case is described, shown 16. For sake of semplicity, it has been considered a geometry with equal ridges. Fig. 17 represents the transmission line model (TLM) of only half of the transversal section of a six-ridge WG, so it stores half of the total energy), which requires some additional considerations respect to the double-ridge case described in [28]. The TRT

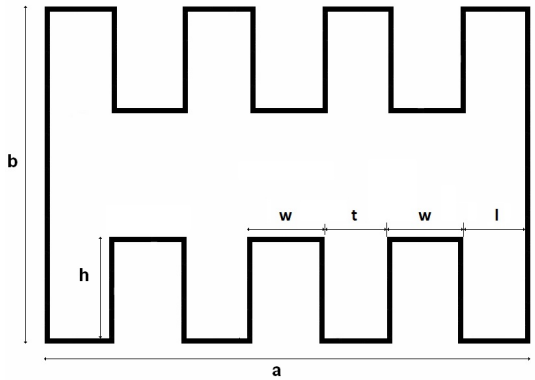

Figure 16: Six ridges waveguide

starts by considering the transversal section of the R-WG as a resonator. The propagation constant is the same for each line (representing a parallel plate section of the R-WG) and it

is equal to the transverse propagation constant k_t, while the impedance is proportional to the WG height. To evaluate the PHC, a voltage V_M corresponding to the maximum electric field is set at the open-circuit (i.e., at the WG center), and an unknown current IS at the short circuit end (i.e. at the WG lateral wall).

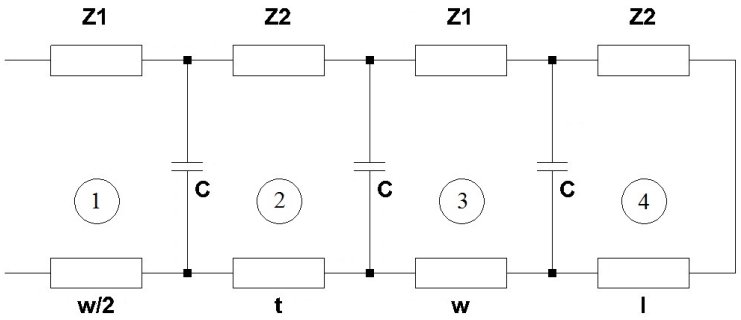

Figure 17: Transmission line model for a 6 ridge waveguide

Letting $l_1 = w/2$, $l_2 = t$, we have

$$\begin{aligned} V_1 &= A_1 \; cos(k_x \; x) \\ V_2 &= A_2 \; cos\left[k_x \left(x - l_1\right)\right] - j \; B_2 \; sin\left[k_x \left(x - l_1\right)\right] \\ V_3 &= A_3 \; cos\left[k_x \left(x - (l_1 + l_2)\right)\right] - j \; B_3 \; sin\left[k_x \left(x - (l_1 + l_2)\right]\right. \\ V_4 &= B_4 \; sin\left(k_x \; x'\right), \end{aligned} \tag{58}$$

where $k_x = k_c = 2\pi/\lambda_c$ and

$$\begin{aligned} A_1 &= V_M & B_2 &= -jZ_2 \; I_{2,in} \\ A_2 &= V_1(w/2) & B_3 &= -jZ_1 \; I_{3,in} \\ A_3 &= V_2(w/2 + t) & B_4 &= -jZ_2 \; I_s. \end{aligned} \tag{59}$$

$I_{2,in}$,$I_{3,in}$ are the input currents at the lines after the conderser nodes.

$$I_1(w/2) = I_{2,in} - jCV_1(w/2),$$
$$I_2(w/2+t) = I_{3,in} - jCV_2(w/2+t), \tag{60}$$

The unknown current I_S can be obtained by imposing the continuity of the voltages at the steps. The electric field is described from the (58) as

$$E_1 = AV_1 \quad E_2 = BV_2$$
$$E_3 = CV_3 \quad E_4 = DV_4, \tag{61}$$

the constant A,B,C,D can be obtained by imposing the voltage continuity at the steps. The same model can be applied to a 3-ridge antipodal WG.

A second way evaluates the power trough the field distribution obtained from the FDFD. The electric field in the integral is computed by the E-field distribution on the transverse section given by the FDFD. This distribution is normalised so that $\max(E)$ is equal to the field at the dielectric breakdown (EBD), so actually gives the maximum power.

$$P = W_{EM}\frac{k_z c}{k_0} = \frac{1}{\sqrt{\epsilon_0\mu_0}}\frac{\lambda_0}{\lambda_g}\frac{\epsilon}{2}\int_S E^2 dS$$

The numerical technique is more precise, and it's applicable to every ridged geometry (e.g. the TRT consideration about voltage has no sense in a trapezoidal R-WG). Moreover, Hopfer formula consideres the voltage maximum in the center of the waveguide, which is (approximately) true only for a geometry with centered ridge. The picture 18 shows the difference between the Hopfer's analytical fomula (red line) and the numerical evaluation (blue) for different geometries of a double ridge waveguide. It can be seen that the curves diverge only for narrow ridges and congerve as the ridges become wide.

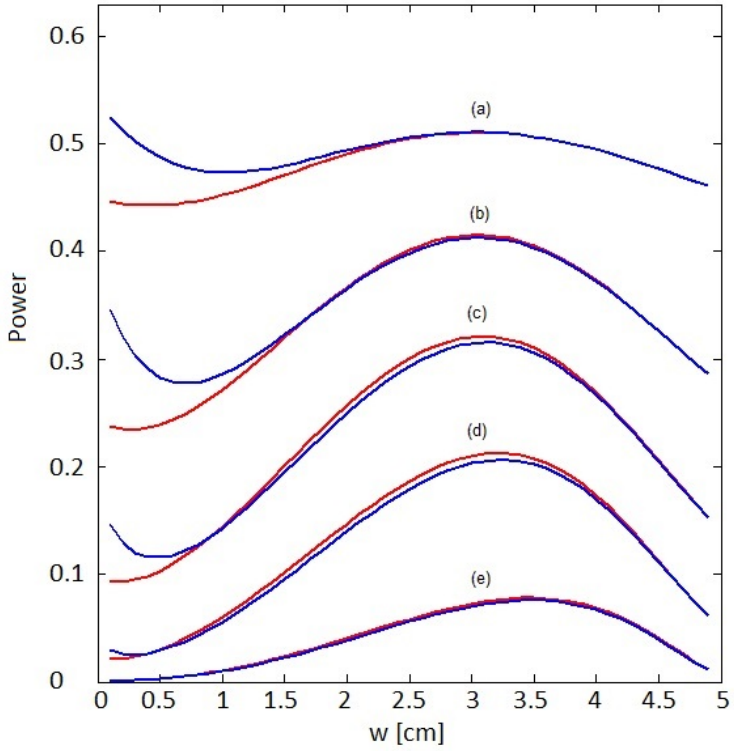

Figure 18: Power evaluation with Hopfer's (red) and numerical (blue) tecniques for a double rectangular ridge waveguide with dimension (axb) 0 (5x2) cm for h=1mm (a), h=3mm (b), h=5mm (c) h=7mm (d), h=9mm (e)

8 Attenuation

The power losses in a real waveguide is due to two contributions. The finite conductivity of the metallic conductor causes that the surface current penetrate in the walls. Moreover the dielectric material which fills the guide can present a loss, so a fraction of the power which flows in the guide is diffused. Both the terms causes a power dissipation and thus a mode attenuation, if this is relevant it cause a coupling between the modes. In this work only the power losses due to the finite conductibility of the metallic conductor are considered, since the WGs are hollow. Power attenuation on the conductor walls is defined as

$$\alpha = \sqrt{1 - \frac{k_t^2}{k_0^2(f_m)}} \frac{1}{2\sigma\delta_d Z} \left[\frac{1}{k_t^2} \int_C |\nabla_t \phi_0(\underline{t})|^2 dl + \frac{k_t^2}{k_z^2(f_m)} \int_C |\phi_0(\underline{t})|^2 dl \right]$$

where f_m is the central frequency in the monomodal bandwidth.

In terms of implementation, this results in a directional derivative along the metallic conductor of the potential computed through the FDFD to evaluate the gradient $\nabla_t \phi_0(\underline{t})$ along the edges of the waveguide. The first integral is computed trough the trapezoidal rule, the second with the rectangle method.

9 Optimization

As it has been said in the previous paragraphs, the ridged geometry increases the mono-modal bandwidth of the structure but reduces power handling capability, so this issue can limit their use. In order to get an effective trade-off between these two conflicting requirements, a suitable optimization procedure should be devised. It has been chosen to use the PSO algorithm as optimizer, developed in MATLAB. The optimization tool must be linked to a suitable model of electromagnetic analysis to allow the evaluation of the performance in terms of bandwidth, PHC and attenuation on the metallic conductor. The picture (19)shows the integration of the EM analysis in the PSO algorithm.

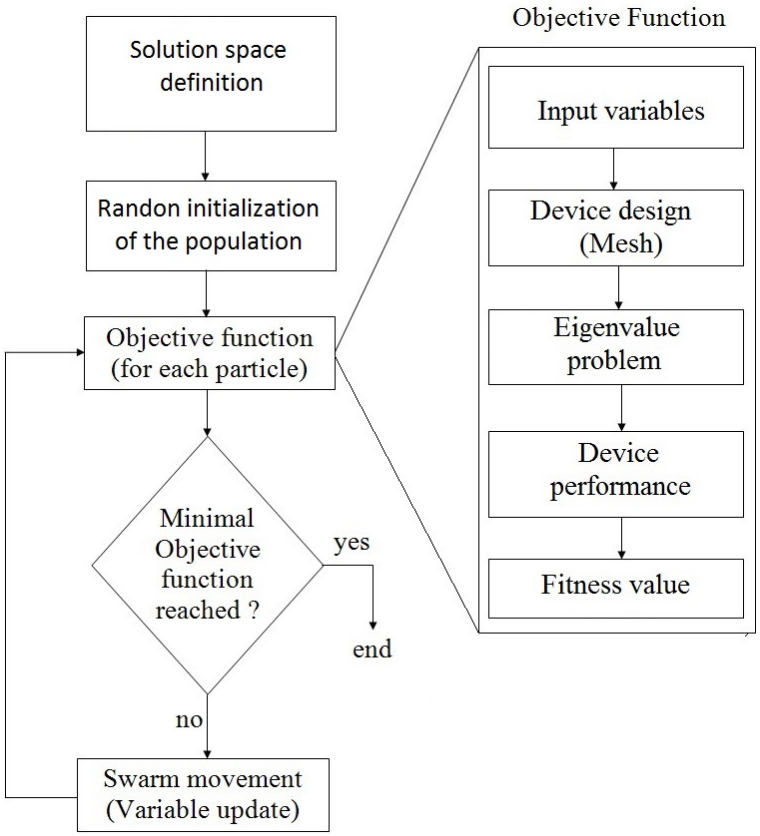

Figure 19: Optimization scheme

The PSO variables to be optimized and which constitute the vector x are the geometric parameters of the ridges: dimensions (width and height) and position (for the multi-ridged geometries), expressed in terms of nodes on the TE grid. They are iteratively modified by the algorithm to find the optimal geometry according to the request. The objective function (o.f.)

describes the request we want to achieve with the optimal geometry, and evaluate how each geometry described by the swarm is suitable to the requests. To do this, the o.f. creates a discrete modelization of the transverse section of the guide, and with an electromagnetic model evaluates the propagation characteristics of the ridge WG, whose parameters are described by the PSO particle coordinates.

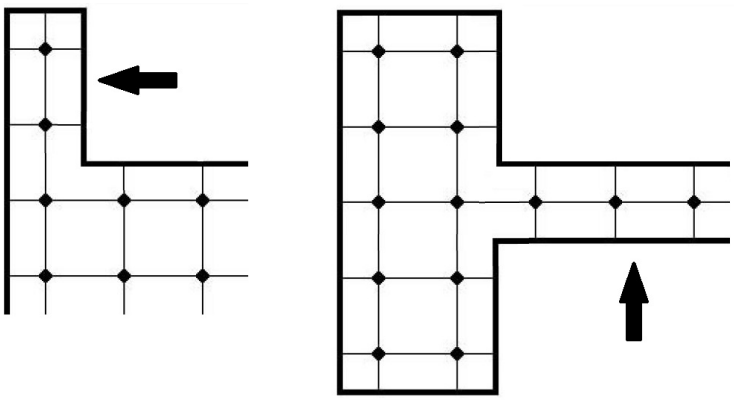

Figure 20: Singularities and forbidden geometries

Each dimension can vary from the minimum length set by resolution (grid node distance) to the maximum dimension which allows the eigenvalue problem to be solved. As a matter of fact, a structure one node wide (see fig. 20)will cause a singularity in the eigenvalue problem. But also a structure two nodes wide doesn't allows as accurate solution. It is clear that the chose of the objective function is one of the most important step of the project.

9.1 Convergence test

The behaviour of a R-WG in terms of BW is rather well-known. Some preliminary optimization of $f(\infty)$ (i.e. BW-only optimization) have been then performed to evaluate the convergence properties of our approach. Since the solution space is discrete, we assume as convergence criterion the equality of the best and worst fitness values of the swarm. By considering a WG with size $(a \times b) = (5 \times 2)cm$ with a discretization step of 0.1 mm; a test on a configuration with a symmetric double ridge leads to the result that the largest BW requires the highest possible ridges ($h = 0.99cm$) with a large width ($w = 1.92cm$). This optimum is always obtained using different c_1, c_2, np values and starting point, since no traps are present. The smaller ci's, the more rapid the convergence: for np = 5, the convergence require about 80 steps for $c_1 = c_2 = 1.5$, and about 100 steps for $c_1 = c_2 = 2$. A similar behaviour has been

obtained for larger np. On the other hand, a larger ci's allow to better explore the solution space, and therefore to escape more easily from traps. The increase in the computational cost is quite small and, since the introduction of the PHC constraints modifies the topology of the solution space and can introduce some local minima (i.e. traps) we have, in the following, chosen $c_1 = c_2 = 2$.

Then, the dependence of the optimization on the number of particles of the swarm has been tested. A typical value for np is 1.5 to 2 times the number of optimization variables. Of course, for the simple cases involving only two variables, we have taken np ≥ 5. It appears that a significant increase of np introduces no reduction in the number of iterative steps. Even worse, this number usually increases a little bit (10-30 % in the cases we have tested). Therefore, it has been concludes that the typical value of np quoted above is also the more effective.

As regards the other parameters of the algorithm, it has been chosen a velocity clamping equal to $\alpha = 0.5$ and a linear decreasing inertia weight w from 0.9 to 0.4. The absorbing wall has been chosen as boundary condition.

10 Rectangular waveguide

The first study focused on a simple bandwidth optimization of rectangular waveguides [3], comparing different geometries. The results showed which shape provides the best bandwidth improvement.

Named

$$b_0 = \left(\frac{f_0}{c/(2a)}\right)^2 \qquad b_0 = \left(\frac{f_1}{c/(a)}\right)^2$$

the cutoff frequencies for the ridge waveguide normalized to the rectangular one, the objective function was chosen as

$$f = \frac{1}{b_1 - b_0}$$

The test considered a standard waveguide (6 x 2 cm) has been discretized using a TE grid, with a discretization step equal to 0.1 mm with respectively with two, four and six simmetric ridges centered along the width of a rectangular WG. As it was expected, the 2-ridge configuration is the only one which provide an improvement in terms of bandwidth. It follows that, when only the bandwidth is the requirement, more than two single ridges are of no utility.

A second study [4] introduced the conflicting requests by using a simple objective function which consisted of a weighted sum of the BW and PHC normalized to their values computed for a rectangular waveguide with the same side dimensions. A simple double ridge geometry and a single "staircase" one have been considered. The objective function has been modeled as

$$f = \frac{1}{P - c(b_0 - b_1)}$$

where P is the maximum power the WG can handle. The parameters c weights between the 2 requirements. It has been shown how varying the relative weight between the requirements of a large bandwidth, and a good power handling capability, the algorithm finds quite different optimal solution. The third work [5] has been developed an objective function that allow the trade-off between conflicting request: the base idea is maximize a request limiting the other one. In this case it has been selected an objective function 62 able to maximize the bandwidth for a fixed power reduction. the bandwidth is maximized.

$$f(k) = \left| \frac{\frac{P_{rect}}{k} - P_{ridge}}{P_{ridge}} \right| + \left| \frac{BW_{rect}}{BW_{ridge}} \right|^2 \tag{62}$$

Such a formula maximizes the BW with a constraint on the power decrease (k-time reduction with respect to the rectangular WG). It has been usually chosen k = 2.0; 3.0, so that the objective function tries to optimize the BW with a maximum power reduction equal to 50% or 66%. Fig. 21 shows the geometries consider in this work. A first test investigates

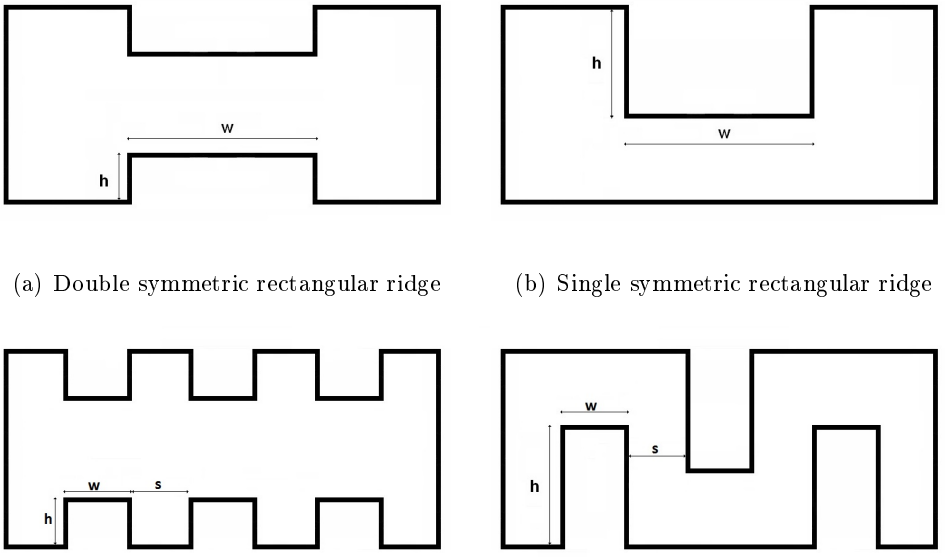

(a) Double symmetric rectangular ridge (b) Single symmetric rectangular ridge

(c) Six symmetric rectangular ridge (d) Antipodal symmetric rectangular ridge

Figure 21: R-WG configuration optimized in [5]

the best solution between a single (configuration (a)) and a double (b) ridge configuration to achieve a bandwidth improvement by using ridges placed at the center of the long sides. The optimum BW is compared with the best one obtained with no PHC constraints, which is equal to 6.7726 GHz (i.e. $BW_N = 2.711$), but in this case the maximum power flux is very small respect to P_{rect}.

A single ridge presents (table 2) a lower improvement in terms of bandwidth respect to the 2-ridges case (table 1). Second test considered the effect of side ridges. The configuration 3 does not work for the equal ridges case: as expected, large side ridges prevent the BW improvement, so the algorithm tends to remove them and the geometry tends toward an unridged WG. Regarding the case with different ridges, the symmetry of the fundamental

$f(k)$	w	h	BW	BW_N
$f(2)$	210	39	3.0698	1.2288
$f(3)$	198	54	3.4218	1.3697

Table 1: R-WG: configuration a

$f(k)$	w	h	BW	BW_N
$f(2)$	170	73	2.9983	1.2002
$f(3)$	158	103	3.2852	1.315

Table 2: R-WG: configuration b

$f(k)$	w_c	h_c	w_s	h_s	s	BW	BW_N
$f(2)$	192	76	194	48	7	3.4812	1.3934
$f(3)$	174	72	192	31	18	3.6682	1.4683

Table 3: R-WG: configuration c

$f(k)$	w_c	h_c	w_s	h_s	s	BW	BW_N
$f(2)$	112	91	20	32	211	3.2485	1.3003
$f(3)$	118	93	18	10	203	3.2655	1.3071

Table 4: R-WG: configuration d

mode allows to simplify the problem to a symmetric structure with respect to its two axes: it has been considered a geometry whose central ridges (w_C, h_C) vary independently from the side ones (wS, hS), moreover the spacing between the ridges s is chosen another parameter to be optimized. The solution space has therefore 5 dimensions and the optimized geometries (obtained with np = 20 particles in the swarm) are shown in table 3. A comparison with table 1 shows a significant BW improvement (for a given PHC) due to the additional (optimized) side ridges. As a further analysis of the side ridges effect, we consider an antipodal geometry (configuration 4), where the two external ridges are equal and equally spaced from the central one. Such configuration can also be obtained by adding two lateral ridges to configuration 2 on the un-ridged side. Since the ridge spacing is also an optimization variable, the solution space has again 5 dimensions, and we used np = 20 in the tests. Table 4 displays the performance

of this geometry.

In both cases, the lateral ridges are small and distant from the central one and, unlike the configuration 2, the central ridge does not cross the horizontal axis of the WG. It is apparent from table 4 that the antipodal configuration allows a BW improvement when a relatively loose constraint on PHC is set. For the tested case, a constraint of 50% reduction in power gives an improvement in BW around 10%. On the other hand, when a small PHC is required, the single ridge geometry is preferable. The side ridges affect the bandwidth improvement in the antipodal geometry, on the ohter improve the BW in the 6-ridge one. So, among the different geometries presented, the 6-symmetric ridge geometry results to be the best solution in term of bandwidth.

Finally [6] extendend the study about the power constraints to the bandwidth maximization for a given attenuation increase. To devise the objective function, the ratio between the actual R-WG properties and the rectangular WG ones has been considered as regards bandwidth, PHC and losses

$$R_B = \frac{B_{rect}}{B_{ridge}} \qquad R_P = \frac{P_{rect}}{P_{ridge}} \qquad R_\alpha = \frac{\alpha_{rect}}{\alpha_{ridge}} \tag{63}$$

As regards the trade-off solutions, the chosen objective function limits the power reduction (or the attenuation increase) respect to a WG without ridges and provides the maximum bandwidth that can be reached with that reduction. The following functions

$$f_P(k) = \left| \frac{R_P}{k} - 1 \right| + R_B^2 \tag{64}$$

and

$$f_\alpha(k) = \left| k - \frac{1}{R_A} \right| + R_B \tag{65}$$

have been selected to maximize the bandwidth with a k-times reduction in PHC (f_P), or with an increase in attenuation (f_α), respect to a rectangular WG (e.g. k=1.1 limits to a 10% increase).

Different R-WG configurations have been considered (fig. 22):

a) a standard double R-WG structure with two symmetric ridges centred along the width of a rectangular WG.

b) a double-trapezoidal R-WG structure with the ridges centred along the width of WG.

c) a singled 3-step "staircase" R-WG structure with ridges centred along the width of WG.

d) a double 3-step "staircase" R-WG structure with ridges centred along the width of WG.

e) a double depressed-rectangular R-WG structure.

f) a double depressed-trapezoidal R-WG structure with the ridges centred along the width of WG.

All configurations have been tested with 20 particles in the swarm, with constant accelerations equal to $c_1 = c_2 = 2$. In our tests, we have optimized the bandwidth respect to a power reduction by a factor 2 and 3, thus considering $f_P(2)$ and $f_P(3)$, and respect to an attenuation increase by a factor 2 and 5, i.e., using $f_\alpha(2)$ and $f_\alpha(5)$.

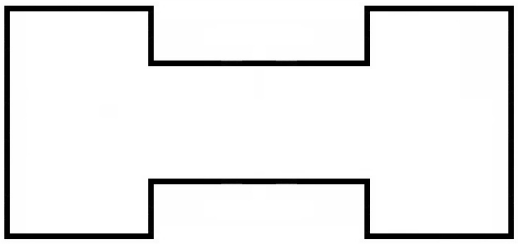

(a) Double symmetric rectangular ridge

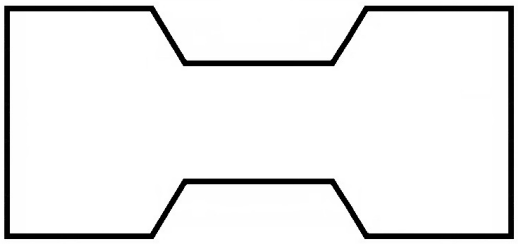

(b) Double trapezoidal ridge

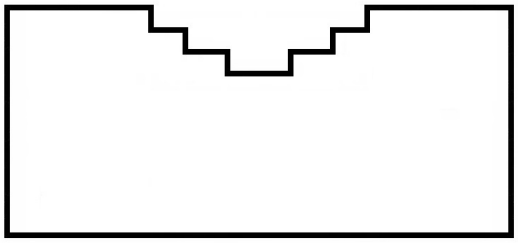

(c) Single staircase ridge

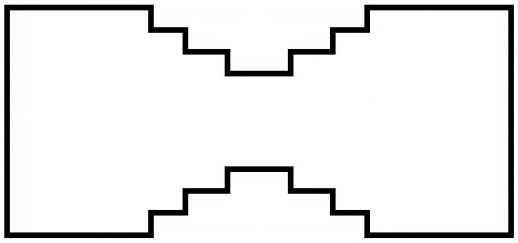

(d) Double staircase ridge

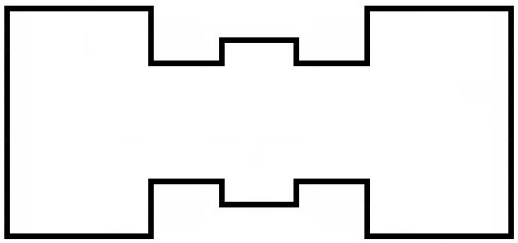

(e) Double depressive ridge

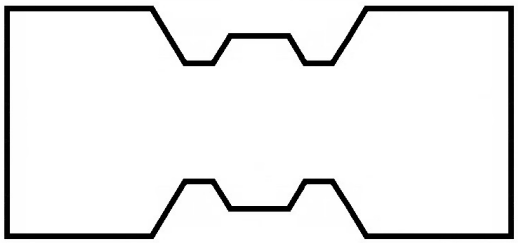

(f) Double trapezoidal depressive ridge

Figure 22: Geometries and variables of the analysed configurations

10.1 Convergence analysis

In order to understand the properties of the chosen approach, the graphs of the R-WG behaviour for a twin-ridge R-WG are shown in the following pictures, as a function of the width (horizontal axis) and height (vertical axis) of the ridges for a waveguide with dimensions $(a \times b) = (5 \times 2)cm$. As it was expected, a good bandwith improvement (fig. 23) requires quite big ridge: the maximum is obtained for the maximum height allowed.

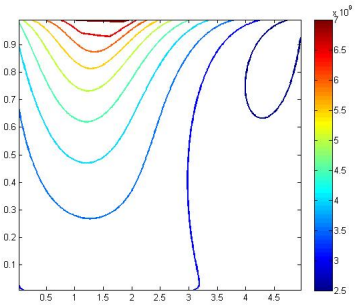

Figure 23: Graphs of the objective functions for simple requests: bandwidth

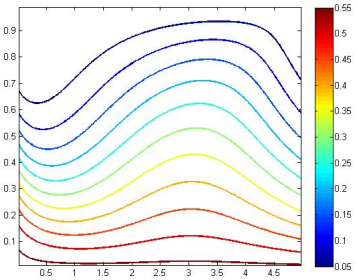

Figure 24: Graphs of the objective functions for simple requests: power handling

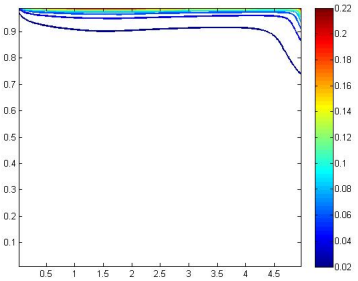

Figure 25: Graphs of the objective functions for single requests: attenuation

The power handling capability (fig. 24) is reduced by the ridge and it decreases as the ridge dimensions increase. Attenuation (fig. 25) increases as lenght of the conductive walls increases, that is, as the ridge size increases. So, the desired performances, namely a low PHC reduction and a low attenuation, have likely behaviour, which is opposite to the bandwidth one.

From these graphs is clear why a trade-off is necessary. Such functions have been combined to obtain a suitable objective function which describes the desired trade-off. Fig. 26 show the objective functions (64) chosen in our work for the power reduction limitation for $k = 2$ (left) and $k = 3$ (right), and it appears that a trade-off between conflicting requirements is actually obtained. Similarly, the picture 27 show the graphs of the objective functions (65) chosen for the attenuation limitation for $k = 2$ (left) and $k = 5$ (right). The results of the optimization, shown in table 5, confirm the outcome of these graphs.

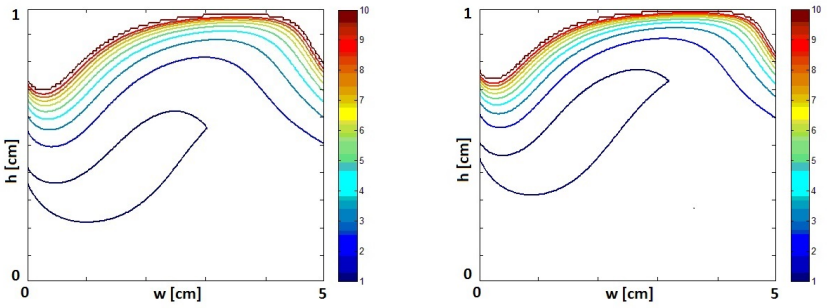

(a) $f_P(2)$ (b) $f_P(3)$

Figure 26: Objective functions for PHC-BW trade-off

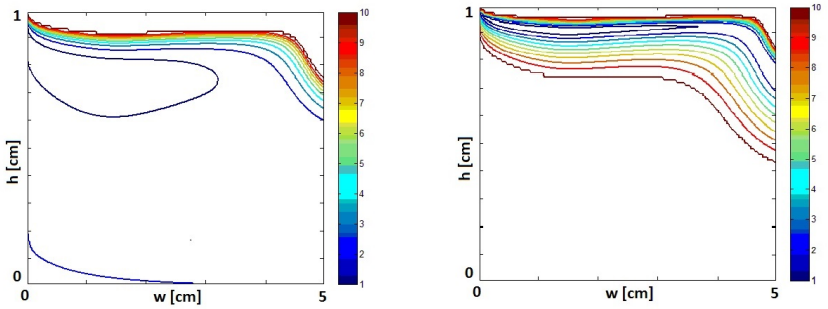

(a) $f_\alpha(2)$ (b) 5 α

Figure 27: Objective functions for α-BW trade-off

The convergence of the swarm is shown in fig. 29, **??**, 30: all the particle converge to the same

minimum value of fitness. The maximum power and the bandwidth are shown to demonstrate that $f_P(k)$ actually minimizes the bandwidth with the requested constraint on the power.

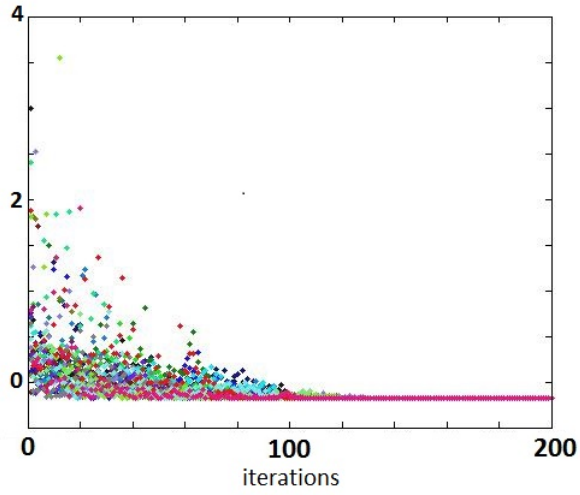

Figure 28: Fitness convergence for case "1/2 PHC optimization"

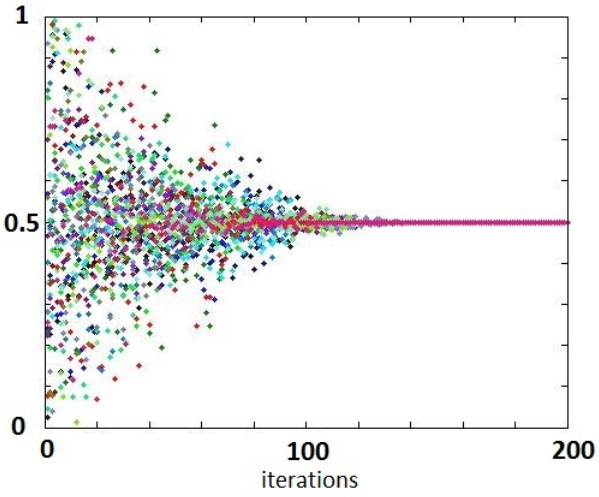

Figure 29: Power convergence for case "1/2 PHC optimization"

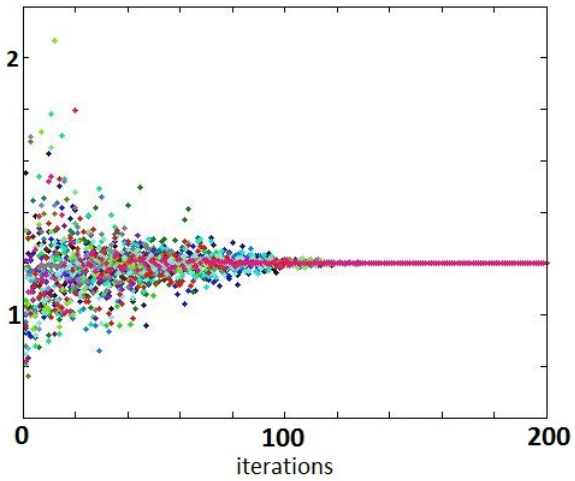

Figure 30: Bandwidth convergence for case "1/2 PHC optimization"

10.2 Results

Rectangular ridges The variables to be optimized are the width and the height of the ridges, which are centered along the long side of the WG. The results of table 5,6 has been obtained either assuming equal ridges and assuming unequal ones.

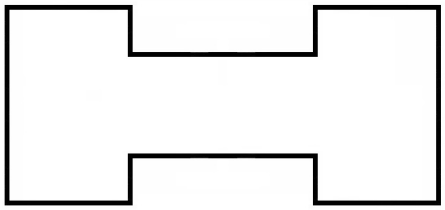

Figure 31: Rectangular ridge in rectangular waveguide

f	w	h	BW	BW_N	PHC	PHC_N
$f_P(2)$	1.64	0.38	3.6760	1.2262	0.2819	0.5000
$f_P(3)$	1.54	0.52	4.0596	1.3542	0.1880	0.3336

Table 5: Rectangular double ridge : PHC-BW optimization

f	w	h	BW	BW_N	α	α_N
$f_\alpha(2)$	1.22	0.76	5.1579	1.7205	0.8413	2.0303
$f_\alpha(5)$	1.14	0.91	6.2211	2.0752	2.0971	5.0609

Table 6: Rectangular double ridge : α-BW optimization

Trapezoidal ridge waveguide The structure has been tested for symmetric (the two ridges have the same dimensions) and asymmetric geometry (the ridges' dimensions are independent): the algorithm has 3 variables in the first case (width, height of the ridge, and slope of the diagonal sides) and 5 in the second. If the variables describe an incoherent geometry (e.g. the trapezoid converges to a triangle) the geometry is discarded by assigning an high value to the fitness. Moreover, the diagonal side has requested a variable different discretization step along the long side, proportional to the slope.

The optimal structures are shown in tables 7, 8, 9, 10.

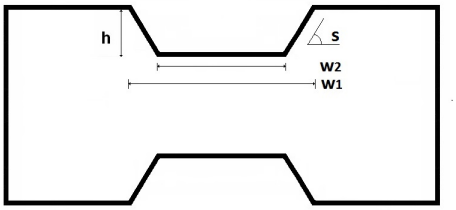

Figure 32: Trapezoidal ridge in rectangular waveguide

f	w_1	w_2	h	slope	BW	BW_N	PHC	PHC_N
$f_P(2)$	1.875	1.4543	0.36	31°	3.6607	1.2211	0.2830	0.5020
$f_P(3)$	2.1802	1.439	0.52	36°	4.0122	1.3383	0.1878	0.3331

Table 7: Trapezoidal double ridge - symmetric: power - BW optimization

f	w_1	w_2	h	slope	BW	BW_N	α	α_N
$f_\alpha(2)$	2.4066	0.6431	0.86	46°	5.7157	1.9066	0.8299	2.0030
$f_\alpha(5)$	2.3181	1.0916	0.92	34°	6.6875	2.2307	2.0705	4.9968

Table 8: Trapezoidal double ridge - symmetric: $\alpha - BW$ optimization

f	w_{1u}	w_{2u}	h_u	w_{1d}	w_{2d}	h_d	slope	BW	BW_N	PHC	PHC_N
$f_P(2)$	1.83	1.42	0.38	1.86	1.50	0.34	29°	3.6624	1.2217	0.2820	0.5003
$f_P(3)$	1.89	1.45	0.48	1.91	1.42	0.54	25°	4.0302	1.3443	0.1878	0.3332

Table 9: Trapezoidal double ridge - asymmetric: power - BW optimization

f	w_{1u}	w_{2u}	h_u	w_{1d}	w_{2d}	h_d	slope	BW	BW_N	α	α_N
$f_\alpha(2)$	2.85	0.51	0.92	2.51	0.03	0.98	52°	5.8589	1.9543	0.8383	2.0039
$f_\alpha(5)$	2.37	1.06	0.98	2.39	1.24	0.86	34°	6.7038	2.3262	2.0714	4.9999

Table 10: Trapezoidal double ridge - asymmetric: α - BW optimization

Staircase rectangular ridge waveguides The structure with a single 'staircase' ridge requires 6 variables in the PSO algorithm. The structure with a double staircase ridges has been tested for symmetric and asymmetric geometry: the algorithm has 6 variables in the first case and 12 in the second. The constraint of ridge gradually narrower is obtained by

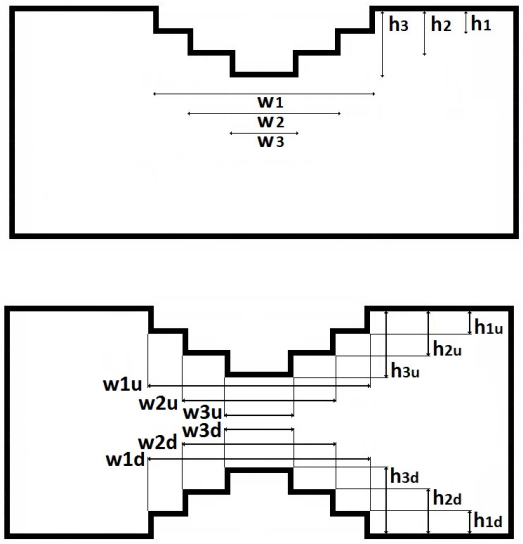

Figure 33: Single and double staircase ridge in rectangular waveguide

using as PSO variables two suitable coefficients which scale the width of a ridge respect to the upper one. A similar method is used to scaling the heights. The correct scaling of the variables has been obtained by choosing as variables the ratio to the upper ridge part: table 11 shows the constraints on the PSO variables.

w1 = w		$6\ \Delta x \leq w \leq a - 4\ \Delta x$
w2 = A w1	$A \in [0.01 : 0.99]$	$4\ \Delta x \leq w_2$
w3 = B w2	$B \in [0.01 : 0.99]$	$2\ \Delta x \leq w_3$
h1 = C h2	$C \in [0.01 : 0.99]$	$\Delta y \leq h_1$
h2 = D h3	$D \in [0.01 : 0.99]$	$2\ \Delta y \leq h_2$
h3 = h		$3\ \Delta y \leq h_3 \leq b - 2\ \Delta y$

Table 11: Constraints of staircase geometry

Tables 12, 13 show the performance of the optimized structure for a single ridge geometry; tables 14, 15, 16, 17 report the results for the double ridge geometry, for the symmetric and the asymmetric configuration.

f	w_1	w_2	w_3	h_1	h_2	h_3	BW	BW_N	PHC	PHC_N
$f_P(2)$	1.20	1.18	1.16	0.01	0.02	0.09	3.5774	1.1933	0.2816	0.4996
$f_P(3)$	4.74	1.04	0.98	0.01	0.09	0.96	3.8566	1.2865	0.1881	0.3337

Table 12: Single staircase ridge - PHC - BW optimization

f	w_1	w_2	w_3	h_1	h_2	h_3	BW	BW_N	α	α_N
$f_\alpha(2)$	2.7	2.54	2.52	0.12	0.28	1.56	3.2060	1.0694	0.8300	2.0031
$f_\alpha(5)$	1.00	0.98	0.96	0.01	0.01	1.82	5.9281	1.9774	2.0766	5.0114

Table 13: Single staircase ridge - α - BW optimization

f	w_1	w_2	w_3	h_1	h_2	h_3	BW	BW_N	PHC	PHC_N
$f_P(2)$	1.66	1.60	0.02	0.37	0.38	0.39	3.6732	1.2253	0.2819	0.5000
$f_P(3)$	1.70	1.66	1.54	0.02	0.04	0.52	4.0584	1.3538	0.1879	0.3334

Table 14: Double staircase - symmetric ridge - PHC - BW optimization

f	w_1	w_2	w_3	h_1	h_2	h_3	BW	BW_N	α	α_N
$f_\alpha(2)$	1.34	1.02	0.62	0.69	0.76	0.80	5.3557	1.7865	0.8472	2.0447
$f_\alpha(5)$	2.08	1.52	1.22	0.15	0.78	0.91	6.5006	2.1684	2.0695	4.9943

Table 15: Double staircase - symmetric ridge ridge - α - BW optimization

f	w_{1u}	w_{2u}	w_{3u}	w_{1d}	w_{2d}	w_{3d}	BW	BW_N	PHC	PHC_N
	h_{1u}	h_{2u}	h_{3u}	h_{1d}	h_{2d}	h_{3d}				
$f_P(2)$	2.7	2.52	1.74	2.66	1.7	1.38	3.6068	1.2031	0.2836	0.5031
	0.01	0.04	0.35	0.14	0.41	0.43				
$f_P(3)$	3.52	2.42	1.58	3.80	1.68	1.58	4.0391	1.3473	0.1862	0.3303
	0.01	0.02	0.57	0.02	0.09	0.49				

Table 16: Double staircase - asymmetric ridge - PHC-BW optimization

	w_{1u}	w_{2u}	w_{3u}	w_{1d}	w_{2d}	w_{3d}	BW	BW_N	PHC	PHC_N
	h_{1u}	h_{2u}	h_{3u}	h_{1d}	h_{2d}	h_{3d}				
$f_\alpha(2)$	1.36	1.00	0.44	1.34	1.02	0.48	5.3384	1.7807	0.8328	2.0097
	0.64	0.76	0.83	0.69	0.75	0.79				
$f_\alpha(5)$	4.92	1.86	1.44	4.18	1.54	1.16	6.4580	2.1542	2.0743	5.0060
	0.01	0.15	0.73	0.01	0.76	0.16				

Table 17: Double staircase - asymmetric ridge - α-BW optimization

Depressed-ridge waveguides The geometries are designed similarly to the staircase ridge: the PSO variables are two geometric parameters ($w,\ h$) and a set of coefficients to scale the others dimensions (see table 18). The results displayed in tables 19, 20 show that depressed

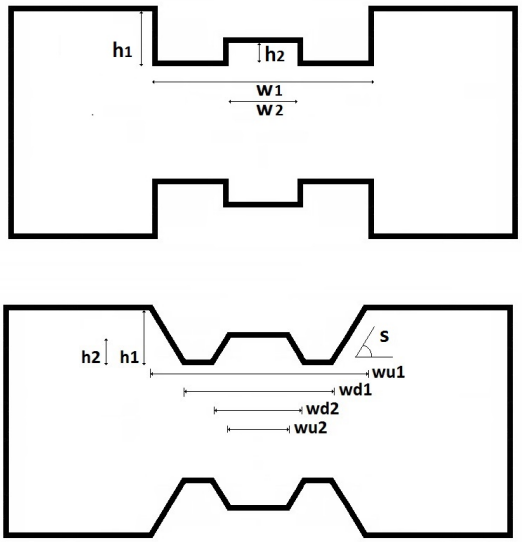

Figure 34: Single and double depressed ridge in rectangular waveguide

ridges don't provide advantages compared to the simple double ridge waveguide in terms of bandwidth (the algorithm tends to eliminate the central 'corrugation'), so no trade-off study has been done.

w1 = w		$6\ \Delta x \leq w \leq a - 4\ \Delta x$
w2 = A w1	$A \in [0.01 : 0.99]$	$4\ \Delta x \leq w_2$
h1 = h		$\Delta y \leq h \leq (b - 2\ \Delta y)/2$
h2 = B h1	$B \in [0.01 : 0.99]$	$2\ \Delta y \leq h_2$

Table 18: Depressed ridge constraints

	w_1	h_1	w_2	h_2	BW	BW_N	α	α_N
BW	1.90	0.99	0.02	0.01	7.1086	2.3712	-	-
α	0.28	0.26	0.21	0.06	3.2182	1.0435	0.3989	0.9507

Table 19: Depressed rectangular ridge

	w_{u1}	w_{d1}	h_1	w_{u2}	w_{d2}	h_2	slope	BW	BW_N	α	α_N
BW	4.3101	1.3650	0.99	0.0297	0.0148	0.01	56	8.2837	2.7632	-	-
α	2.9772	0.3091	0.99	0.0134	0.2957	0.11	53	6.4581	2.1542	0.0322	0.0777

Table 20: Depressed trapezoidal ridge

11 Sectoral elliptic waveguide

Ridged circular waveguides, ridged elliptic waveguides (REW) and sectoral elliptic waveguides (SEW) can be found in many components like filters, matching networks, orthomode transducers, polarizers and circulators that are widely used in satellite and terrestrial communication systems. Low-cost design, small size, and optimum performance of these components are essential to satisfy the payload requirements. An analytical, closed form solution exists

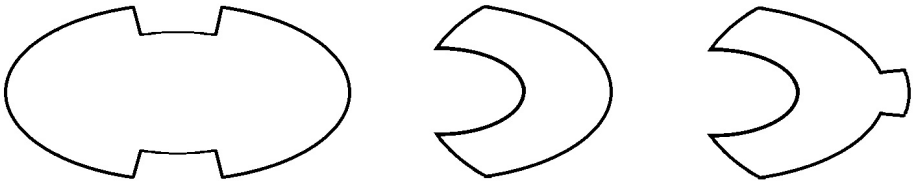

Figure 35: Elliptic ridged waveguides

also for elliptic waveguides, and it has been found by Chu [34] since the 30's. Unfortunately, the field distribution is described by the Mathieu functions [35], whose numerical evaluation is very cumbersome. The best approach seems the expansion of those functions in a series of (more tractable) Bessel functions [36] . In [37] the cutoff wavelengths have been computed efficiently applying by the method of fundamental solutions. In [38], using Mathieu functions and their addition theorem, was presented the general exact solution for evaluation the cutoff frequency in eccentric elliptical waveguides.

The optimization has been applied to the sectoral elliptic waveguides. The structure SEW (see fig. 36) requires six variables in the PSO algorithm.

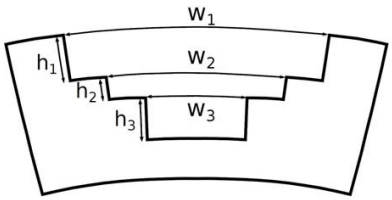

Figure 36: Transverse section of a sectoral elliptic waveguide

As seen for staircase rectangular ridge, the correct scaling of the variables has been obtained by choosing as variables the ratio to the upper ridge part and by imposing the constraints shown in Table 21.

Table 22 summarizes the optimal dimensions and the performance of the considered struc-

$w_1 = w$		$6\Delta v h_{u,v} \leq w \leq (v_2 - v_1)h_{u,v} - 4\Delta v h_{u,v}$
$w_2 = Aw_1$	$A \in [0.01 : 0.99]$	$4\Delta v h_{u,v} \leq w_2$
$w_3 = Bw_2$	$B \in [0.01 : 0.99]$	$2\Delta v h_{u,v} \leq w_3$
$h_1 = Ch_2$	$C \in [0.01 : 0.99]$	$\Delta u h_{u,v} \leq h_1$
$h_2 = Dh_3$	$D \in [0.01 : 0.99]$	$2\Delta u h_{u,v} \leq h_2$
$h_3 = h$		$3\Delta u h_{u,v} \leq h_3 \leq (u_2 - u_1)h_{u,v} - 4\Delta u h_{u,v}$

Table 21: Constraints of SEW geometry

ture of fig. 36 and confirms the effectiveness of PSO.

o.f.	$w_1/h_{u,v}$	$w_2/h_{u,v}$	$w_3/h_{u,v}$	$h_1/h_{u,v}$	$h_2/h_{u,v}$	$h_3/h_{u,v}$	BW
$f_p(2)$	1.19	1.17	1.15	0.01	0.02	0.09	3.55
$f_p(3)$	4.72	1.02	0.99	0.01	0.09	0.94	3.86

Table 22: Results for SEW optimization

12 Discussion of the results and conclusions

As it can be seen from the presented results, the chosen objective functions provide the desired trade-off between two conflicting requirement. An effective limitation in PHC or attenuation is obtained, whereas the bandwidth is maximized by respecting such a constraint. Therefore, such approach is quite effective in the design of ridge waveguides.

As regards the propagation properties, as regards a rectangular waveguide the trapezoidal and rectangular R-WG provide almost the same BW when the PHC is constrained. On the other hand, a wider BW is obtained for trapezoidal ridges when the constraint are set on the power losses. Except for some cases, the staircase geometries have lower performances compared to the trapezoidal ones. This could be intuitive by considering the stair-case ridge as a "discrete" version of the trapezoidal one.

Finally, it is shown how, through a proper modification of the FDFD method for elliptical coordinate (as explained in the chapter 6), it is possible to optimize also WGs with a curvilinear transverse section.

So, the effectiveness of the method has been demonstrated regardless of the mathematical model which describes the structure .

Part III

End-Launcher transitions

In microwave engineering, waveguides (WG) are probably the most widely used propagation structure due to their easy fabrication, high power handling and low losses. Normally, only part of the microwave system employs waveguides. Therefore, a suitable transition is required to connect the waveguide part to the rest of the system. The latter can employ coaxial cables or printed structures, such as microstrip, but high-performances systems have coax connections. Therefore, WG-to-coax transition with a wideband input match and low insertion loss are required. The traditional WG-to-coax configuration has the WG axis orthogonal to the coax axis, but in some receiver system this is not an admissible solution, since the whole transition must have a very small transverse size.

In radioastronomy, a typical feed system consists of a 2-dimensional corrugated horn antenna, marker injector, polarizer and orthomode transducer (OMT), all these devices are either realized in guided wave technology. The two parallel outputs of OMT match the two circular polarizations (RHCP and LHCP). These two output signals can be excited through a transition, which can be realized through different configurations. In particular, in a composite feed system, e.g. horn antennas in array configuration, the limitation in spacing imposed by the array factor (gain, grating lobes) reflects on the spacing between the waveguide elements [39], so the radiating elements are required to be close and the typical transition cannot be used, but is necessary to used a a colinear end-launcher transition.

This paper analyses the performance of an in-line coaxial-to-waveguide and a microstrip-to-waveguide transitions in Q band (33-50 GHz) designed for the Sardinia Radio Telescope (SRT). Both the models have been designed for a rectangular waveguide WR-22.

13 General design

The transition is a crucial point of the global design for achieve a wideband matching, and it has to guarantee a low insertion loss and high return loss to combine properly the involved components. Moreover, an easy fabrication and a compact design are requested.

Mainly, the transition between two microwave structures has to accomplish two different requests over a large bandwidth: an impedance matching between the two devices and the mode conversion from the TEM mode in the coaxial cable (or the quasi-TEM in the microstrip) to the TE10 in the WG. The impedance mismatch is compensated by a ridge stepped transformer, which reduces the high impedance of the rectangular waveguide to a more easily matchable value with the end-launcher one, which is typically 50 Ohm. The dimensions of such ridges are chosen to satisfy the Chebychev multistep wideband matching (with small modifications to satisfy the reactive effect at the impedance steps) [40]. Such a impedance trasformer must satisfy a trade-off between a good matching (witch requests a multistep geometry) and a very compact structure (as short as possible). A particular geometry completes the design with the mode conversion between the two guiding structures: it consists of matching elements in the two structures to be coupled.

14 Coaxial-cable

First studies about coaxial-to-waveguide transitions has been made by Wheeler [42], who analyses several configurations with a step-ridge transformer. Tang and Wong [43] has applied the in-line configuration for a phased array antenna to improve the radiation impedance characteristics of an element superpositioning of two or more modes. Different solution have been proposed by the scientific community. Deshpande [41] analysed analytically an L-shaped configuration. Such a configuration doesn't request a impedance transformer but it is quite difficult to realize at the considered frequency range. Dix [44] has introduced a procedure to match the waveguide to a 50 Ω coaxial cable on a wideband through a tapered ridge or multi-section one quarter WL-length transformer ridge, which overcome the problem of shorting the coax to the WG.

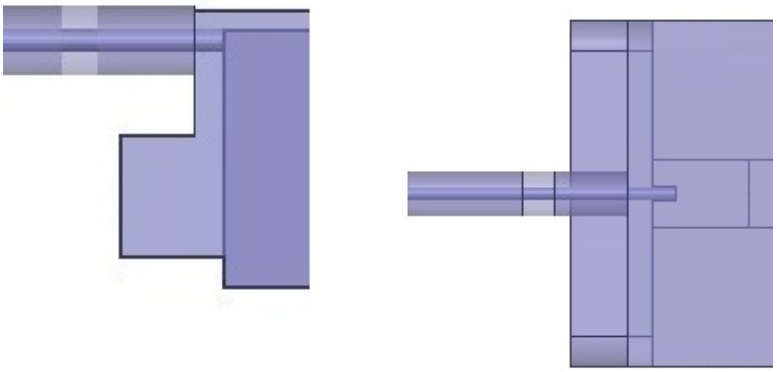

Figure 37: Coaxial cable end launcher: side and top view

The project presented in this work considers a WR-22 (a x b = 5.6896 x 2.8448 cm, ZPV = 488 Ω) and a coaxial cable filled with Teflon (Z=50 Ω). Figures 37 show the top view and side view of the design. The coaxial cable enters at the center of the long side of the WG and it's shifted near to the top of the short one. The first step of the waveguide is modified to allow the mode matching between the two structures (the WG height is reduced, and a backshort is present to allow a better matching) and the inner conductor of the coaxial is shorted to a ridge. Moreover, the input reactance cancellation is achieved by a reactance-series in the coaxial cable. Such a reactance is realized through a discontinuity in the dielectric insulator, the Teflon has been removed at a certain distance from the transition to create a capacitance which balances the reactive parasitic components inside the waveguide. Figure 38 shows the

performance of such a geometry: the return loss is lower than -23 dB in the whole Q band. The order of magnitude of the wavelength in the band Q makes the structure with very small

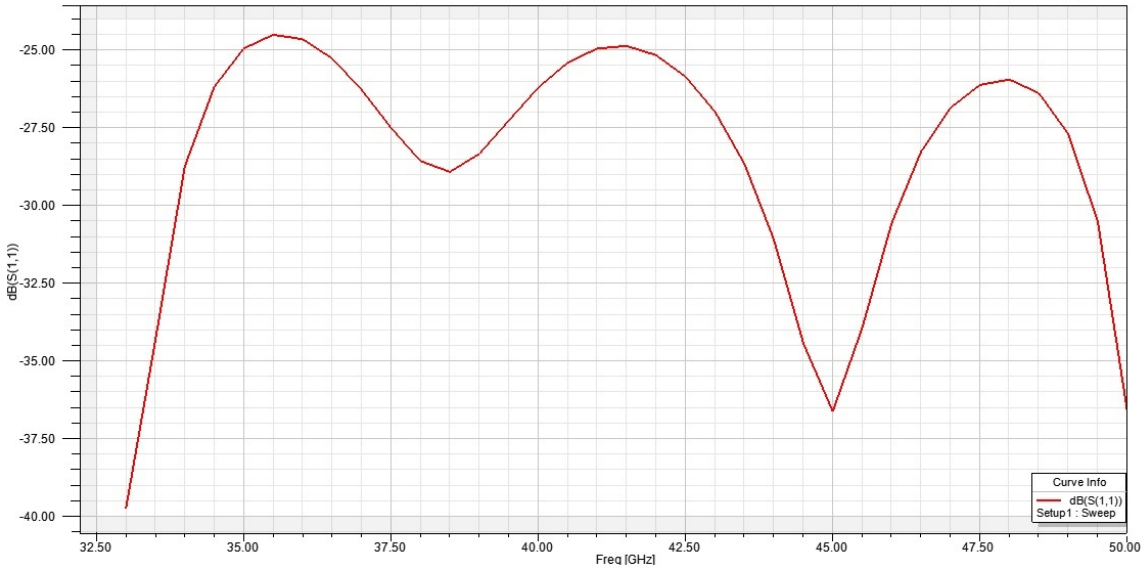

Figure 38: Coaxial cable end launcher: simulation results

dimensions, therefore an high constructive precision is requested. So, the short between the coaxial cable and the ridge is a very critical element. For this reason a modified geometry has been chosen: the coaxial conductor is inserted in a hole created in the first ridge (fig. 39).

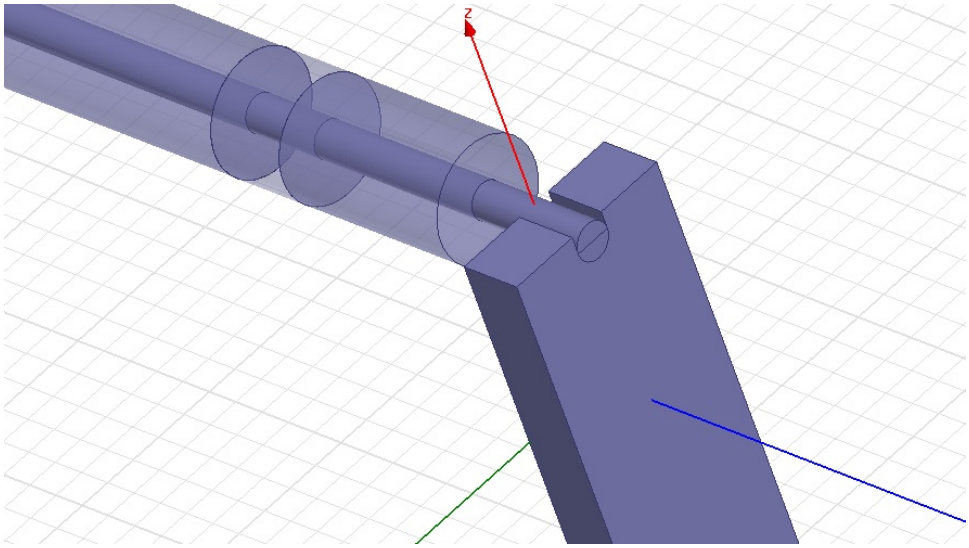

Figure 39: Coaxial cable end launcher: short between the coaxial cable and the ridge

The graph 40 shows the return loss of the second version of the project, which is less than -24dB over all the Q band.

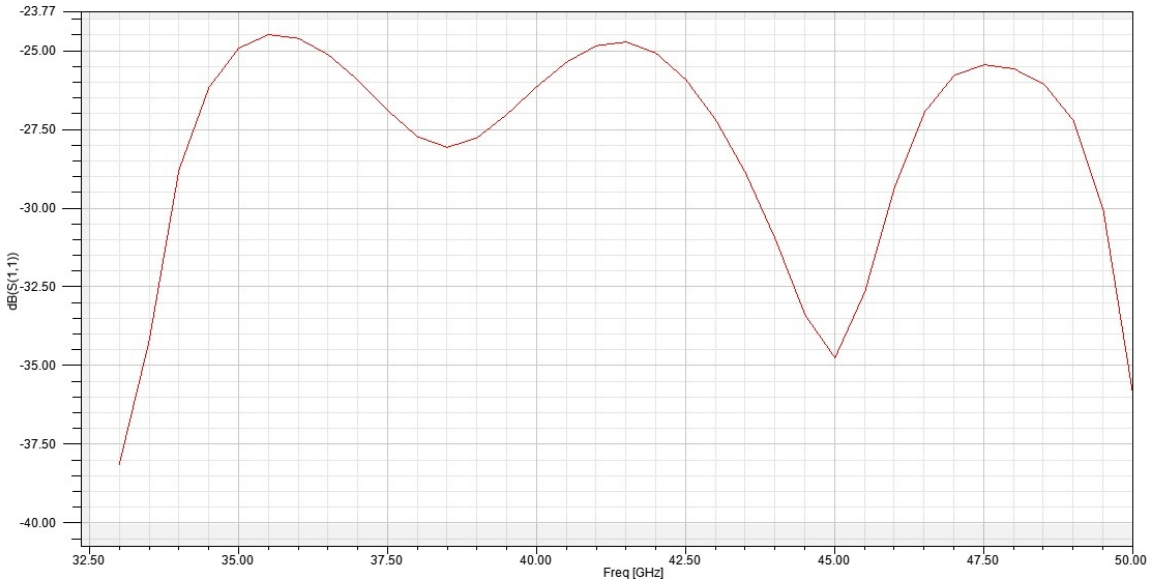

Figure 40: Coaxial cable end launcher: simulation results of the modified geometry

15 Microstrip

Planar technology is widely used in microwave receivers and signal processing for the easy realization, compact size and easy integration with other circuits. A lot of possible configurations of microstrip-to-waveguide transition have been proposed in the last decades, where the probe is an extension of the transmission line which carries the signal.

The inline transitions had been introduced by a full-wave analysis of Yao [45] in 1994. In the following decades other authors proposed alternative design to realize an inline transition between a microstrip and a waveguide. Deslandes [46] presented a particular transition where the waveguide is integrated in the same microstrip dielectric. Zhang [47] proposed a simple assembly which exploits a dielectric-loaded WG.

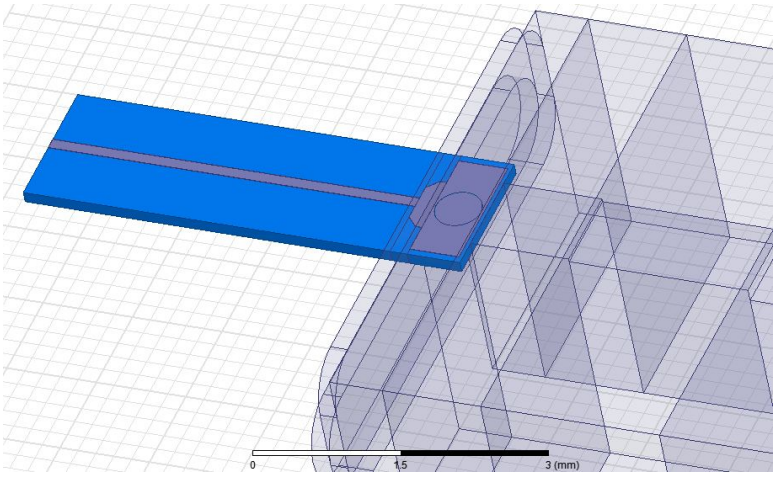

Figure 41: Microstrip end launcher

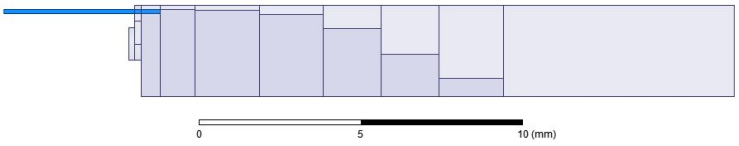

Figure 42: Microstrip end launcher: side view

Figures 41, 42 show the design. The microstrip is realized on an Alumina 98% substrate (thickness 0.127mm, $\varepsilon_r = 9.8$) The dielectric substrate terminates inside the WG on the first ridge, wheres the ground plane doesn't enter inside the WG. The patch is inserted as well as in the coaxial case and it's shorted to the ridge, and it's matched to the 50 Ohm line through a proper transformator. The backshort of the guide is modified to improve the matching, and

a Chebychev stepped ridge completes the structure. Figure 43 shows the performance of this geometry: the return loss is less than -22 dB over all the Q band.

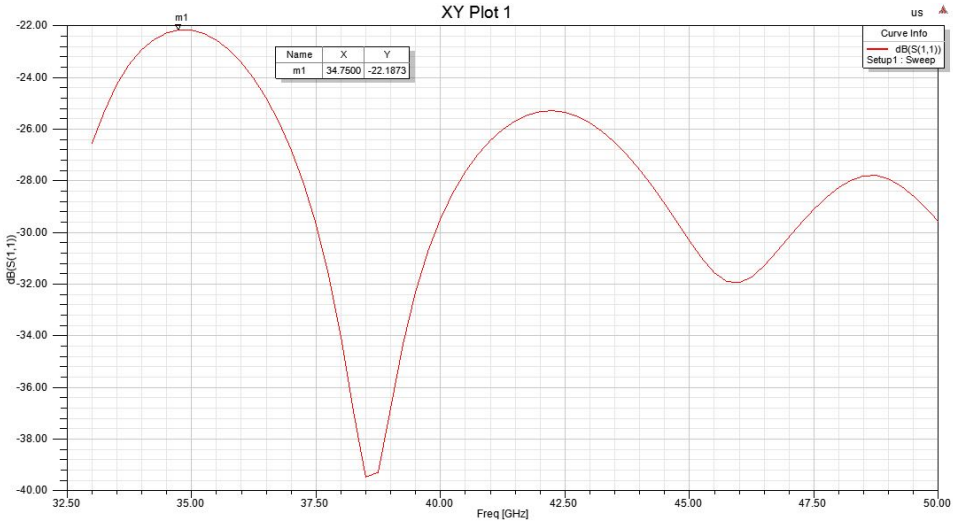

Figure 43: Microstrip end launcher: simulation results

A further step of the project has required the connection of the microstrip feeding structure to a coaxial cable, as shown in fig. 44. This resulted in some modification of the patch and a little matching network along the microstrip. The figure 45 shows the performance of the final structure: the return loss is less than -22.5 dB over all the Q band.

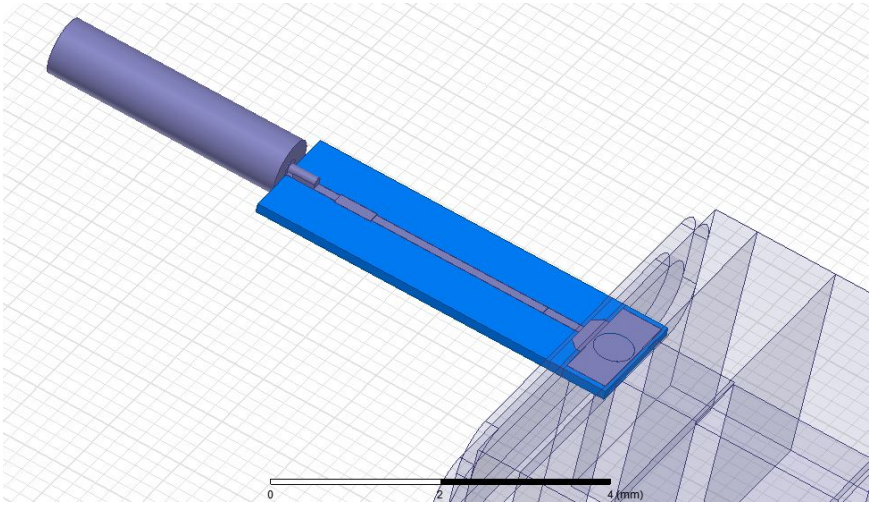

Figure 44: Microstrip end launcher: final geometry

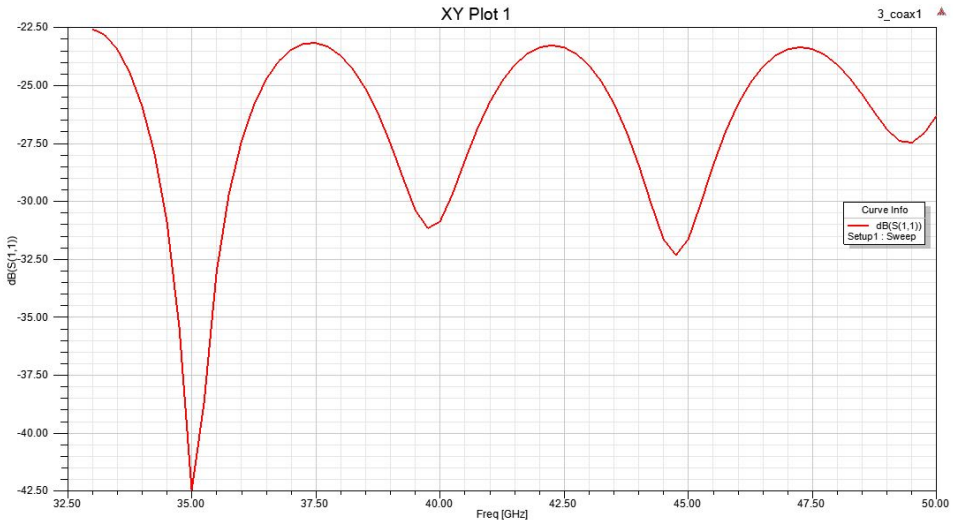

Figure 45: Microstrip end launcher: final geometry return loss

16 Optimization

The design of such a structure can't be brought back to analytical functions or a standard guidelines. Hence, the design not only requires the optmization od the dimension, but most of all the choice of the right geometry which guarantees in the same time the correct operation according to the specific, a easy fabrication, good constructive tollerances and a compact shape. Bacause of this, an automatic optimization of the whole structure not only would request a very large computational load (due to the large number of parameters to be optimized), but would imply a defined geometry. So, it's not the best way to achieve the specifications. Nevertheless, a optimization strategy can be useful to optimize the Chebychev impedance transformer. As it is well known, the larger number of sections are used, the better impedance matching will be achieve over the required frequency range. Ideally, a tapered transformer would provide the best solution. However, the request of a very compact transition results in a fewer possible number of stadium, which implies a very precise project. The Chebichev transformer is described analitycally, and the thoretical values of impedance can be easily obtained. But, the realization of such a transformer by means a series of ridge waveguides has some complications. First, the expressions for the three impedances in a waveguide (Z_{PV}, Z_{PI}, Z_{VI}) are only approximated formula, moreover each discontinuity between two stadiums introduce reactive phenomena which affect the operation. So, by imposing the same width for all the ridges, it is necessary to optimize the heights (which modifies the impedence value) and the lengths (which balance the reactive phenomena) of each step to minimize the return loss. The fist step of the block under test is the ridge where the coaxial or the microstrip is shorted, its height is imposed by the vertical offset of the launcher. A 5 steps trasformer has been chosen, so the variables to be optimized are 10. For a quicker convergence, it has been

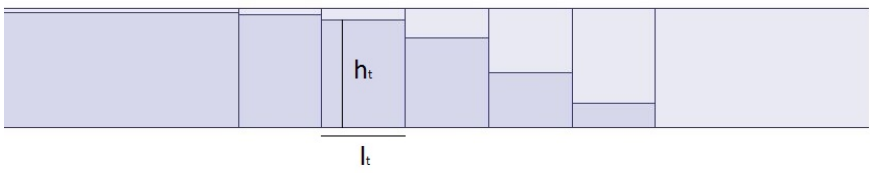

Figure 46: Side view of the impedance transformator

defined such variables starting from the analytic values, and the real optimization variables is a additional correction term. For example, named h_{t*} the height computed for a generical

step

$$h_t = h_{t*} + \Delta h$$

Δh is the PSO variable and h_t is the final height of ther generic step. The same considerations are valid for the lengths l_t

$$l_t = l_{t*} + \Delta l$$

The optimization is obtained following the same strategy described in the chapter 5, by applying the PSO through a synergic operation of Matlab and HFSS. The variable are expressed in millimeters and are truncated to the second decimal place (it has assumed a tollerance of $\pm 10um$). As shown in figure 47, the return loss is less than -25dB over all the Q-band.

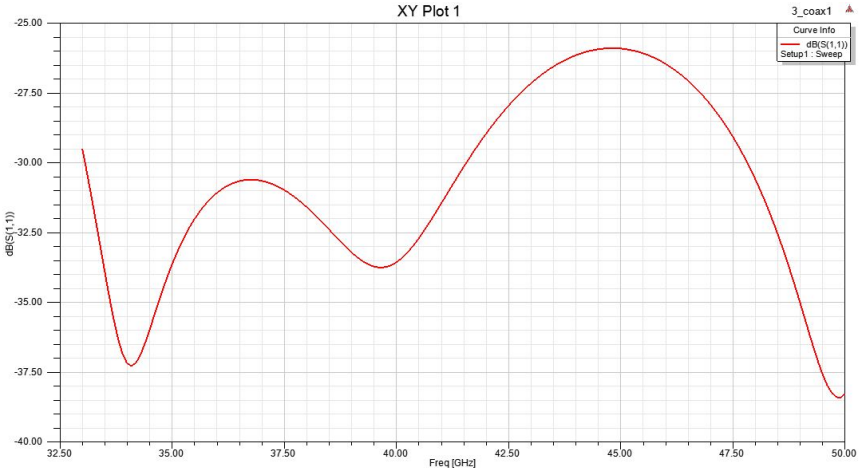

Figure 47: Return loss of the Chebychev impedance transformer

Part IV

Resonant Cavity

Biochemical reactions involves electrical forces between the charged part of the reacting molecules. Chemical binding consists on electrical interactions at microscopic scale. So, an external electromagnetic field can interact with such reactions[67] the stronger is the field intensity, the more significant the interaction is. The widespread diffusion of mobile phones, and any other wireless devices, has risen the interest on the interference of the electromagnetic waves with the biochemical reaction in the human body In the last decades, the widespread diffusion of cellular and wireless systems has made even the general populations aware of these phenomena, since they could result in interference with the biochemical reactions that occur in the human body [68], and a huge amount of research activities has been carried out on this topic.

This interference, however, can be exploited to accelerate several industrial processes by means proper electromagnetic fields. The development of more sustainable processing techniques is one of the most important aims in engineering, chemistry and biochemistry research. An entrance electromagnetic field can accelerate a large number of industrial processes [69], so microwave irradiation has attracted a big attention and has become a widely accepted non-conventional energy source: microwave processes provide a faster heating compared with traditional heating techniques, this results in a faster reaction[70]. Moreover, other advantages sometimes arise, e.g. the possibility of reducing the amount of solvents and of increasing yields and/or selectivities [71], [72], [73].

Basically, an electric field generates heat by two specific mechanisms: dipolar polarisation and ionic conduction. However, many recent studies have showed that chemical and biochemical processes conducted with microwave irradiation often give different results if compared to those obtained with conventional heating working at the same (apparent) temperature [74], [75], [76]. Some authors suggested that the differences in reactivity and selectivity could be due to both thermal-kind (local overheating, hot spots, selective heating) [77] and specific (non-thermal) mechanisms [76],[78]. The latter would derive from a direct and specific action of the electric field on some specific molecules in the reaction medium and would be "measured" through apparent variations in the kinetic frequency factor and/or in the activation energy [79]. However, despite the big efforts made by researchers, a whole accepted reason

why microwave radiation sometimes enhances chemical and biochemical processes has not been reached. In effect, the application of microwave technology in biochemistry has not yet been fully exploited. The main reason of this might be because a precise temperature control is much more difficult in microwave irradiated reactors, while enzymes are very fragile catalysts and cannot be subjected to not well known reaction conditions. As regards enzyme reactions, improved yields that cannot be due only to a thermal effect have been registered in many cases, like isomerase [80] and amylase [81] catalyzed reactions or lypase catalyzed transesterification (for biodiesel production) [82], [83]. However, the mechanism of the modified enzymatic activity (and whether it is thermal or non-thermal) is still unclear. A possible mechanism is that the electric field would lead to orientation effects of dipolar molecules and of active sites of the enzyme, which result in a closer distance and a stricter coordination with the reactive groups in substrate molecules, thereby leading to higher efficiency and specificity in enzymatic reactions [84]. The presence of non-thermal effects during chemical, biochemical and biological processes under microwave irradiation cannot be easily demonstrated, because of the inherent difficulties in conducting such experiments. In fact, non-thermal effects (if they exist) operate concurrently with thermal ones. However, looking at a large part of the literature results, microwave power has not been monitored or was high enough to give a temperature rise in the medium: in these conditions, a quantitative distinction between thermal and non-thermal microwave effects is very difficult or impossible.

The needs of reproducibility and strict control of the operating parameters can be satisfied only with the design of a suitable experimental apparatus. Therefore, in order to evaluate both the possibility and the effectiveness of the use of EM field, the environment must be controlled in terms of chemical (and fluidodynamics) conditions and field distribution. A resonant cavity [85]is a good instrument to study the effect of a uniform electromagnetic field incident on the sample, and with particular symmetric geometries it is possible to irradiate more samples in the same time. Such cavities allow to easily obtain different mode distribution with the required rotational symmetry. A proper design of the cavity requires to take into account also the behaviour of the reagents and their interactions with the electromagnetic fields. However, this has not been done in the literature so far.

The work described here consists on the optimized design and the analysis of a microwave fed resonant cavity (through a power generator which works at 2.45 GHz) suitable for the evaluation of the effect of the electromagnetic exposition on chemical compounds or biological

tissues and of the organic reaction rate.

17 Cavity Design

The device consists on a cylindrical cavity tuned to work at 2.45 GHz (i.e., the frequency allocated for industrial application).

Inside the cavity is present a suitable container to help keep the materials to be exposed in aqueous solution. Moreover, the necessity of a continuous flow of solution in order to test the effectiveness in chemical processes has requested a multi-tube reactor placed inside the cavity. It consists on 8 plexiglas tubes arranged symmetrically respect to the center of the cavity to guarantee a uniform absorption of the electromagnetic radiation by the liquid, as shown in figure 48.

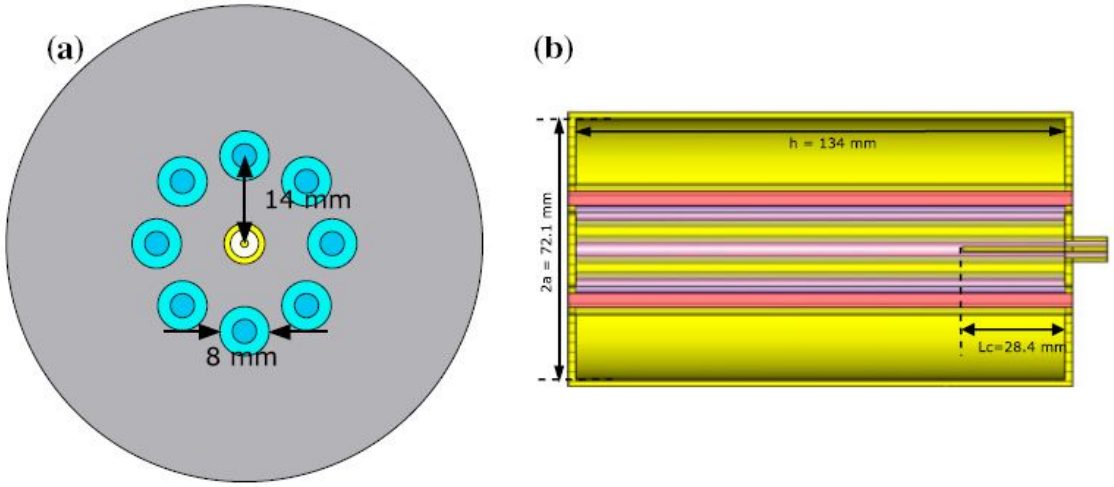

Figure 48: Top and side view of the cavity

An external pumping system has been used, so that the tubes diameter has been chosen as to reduce significantly the dispersion of the field outside the cavity. In the cavity design, the fluid under first test has been modelled as water, because the dielectric properties of the experimental fluid systems are essentially the same as those of pure water.

As a first approximation, it is assumed the cavity filled with a homogeneous material with dielectric permittivity $\epsilon_{r,avg}$, which is the volume weight average of the permittivities of the materials inside the cavity:

$$\epsilon_{r_avg} = \frac{V_a + V_W \epsilon_{rw} + V_p \epsilon_{rp}}{V_a + V_w + V_p} \tag{66}$$

wherein V_a, W_w, and V_p are the internal volumes filled respectively with air, water, and plexiglass, , ϵ_{rw} and ϵ_{rp} are the relative permittivities of water and plexiglass. Let $2a$ is the cavity diameter and h its height. The resonant frequencies of the cavity are obtained by the

equation [85]:

$$f_{nml} = \frac{c}{2\pi a\sqrt{\epsilon_{r_a vg}}}\sqrt{\left(\frac{l\pi a}{h}\right)^2 + x_{nm}^2} \tag{67}$$

where $2a$ and$h$ are the diameter and the length of the cavity, l, m, n are integers, and x_{nm} are the zeroes of the derivative of the Bessel function of the first kind. The fundamental mode correspond to n = 1 and m = 1, for which $x_{nm} = 1.841$. However, a mode independent from the azimuthal coordinate is needed, in order to irradiate in the same way all the tubes. The cavity has therefore been tuned on a higher-order mode, the TM_{012} and the size has been chosen to make it resonate at the frequency of 2.45 GHz. It has been considered a cylindrical cavity, with a diameter $2a = 72.1mm$, and height $h = 102.3mm$ such that the resonant frequency is $2.45GHz$ according 67.

18 Optimization

The above model for the resonant cavity does not take into account the variation of the electric field inside the cavity due to the inhomogeneous distribution of the water. However, it can be a good starting point for the optimization procedure, which has been performed using CST microwave studio. The CST simulation of the full device (cavity and tubes), with the above-mentioned values for a and h, provides a resonant frequency of the TM_{012} mode equal to 3.046 GHz. The discrepancy is due to the inhomogeneous distribution of the electric field, because in 66 the dielectric permittivities of air, plexiglass and water have not been weighted over the electric field distribution inside the cavity. Furthermore, the imaginary part of the loss constant of water cannot be neglected at the frequencies of interest. By considering a lossy Debye model of distilled water [86],it has been used a dielectric tangent at the higher operating frequency (2.45 GHz) equal to $tan\delta = 0.15$. As a consequence, to ensure that the cavity operates at the required frequency of 2.45 GHz, the height h must be increased with respect to the starting value. The full device optimization performed by CST with the new model has provide a final result equal to $h = 134mm$. The S11 performance of the final cavity is reported in Fig. 49. The result shows that the required resonant frequency has

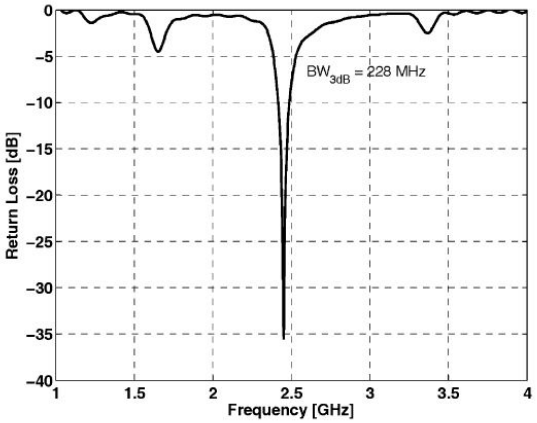

Figure 49: Return loss with probe length Lc = 28.4 mm

been obtained, and the bandwidth is large enough for the applications at hand. However, the electric field distribution is as important as the input match in order to achieve the right exposition of the samples. Fig. 50 and 51 show that field is azimuthally constant at the resonant frequency, as required to irradiate all tubes in the same way. On the other hand, the longitudinal field is not constant but, since the irradiated liquid is flowing, this is not a

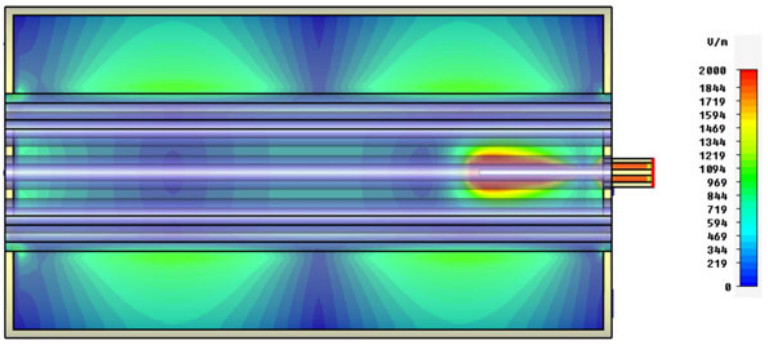

Figure 50: Longitudinal electric field inside the cavity at 2.45 GHz

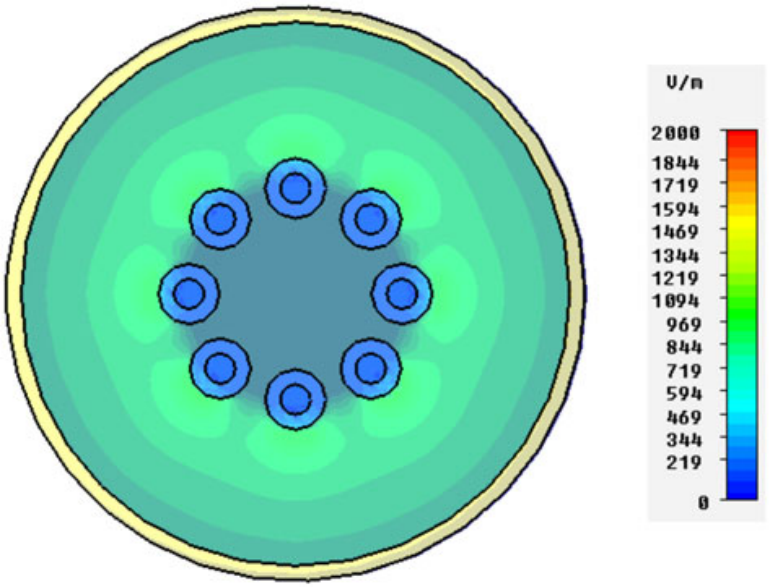

Figure 51: Transverse electric field inside the cavity at 2.45 GHz

problem. Actually, the choice of a flow system, instead of a static one, is due to the need of creating well mixing conditions and so preventing a differential microwave exposition. The dimensions of the flow tubes are of the same order of magnitude than the expected thickness of the exposed fluid and the operating conditions make possible to operate in the laminar flow regime.

Part V

Metaferrites

A Frequency Selective Surface (FSS) is a planar resonant structure consisting on a periodic linear or planar array of identical elements, which has found several applications in electromagnetic technology in the last years. Basically, it is a periodic lattice of conducting strips or slot on a metallic screen and it acts as a filter for the incident wave: a FSS shows different properties at different frequencies. The strips act as electric dipoles and have a stop-band behaviour at the resonance frequencies of the dipoles (the incident wave is reflected near the resonant frequency); the slots act as a band-pass filter, they are transparent to the incident wave at the resonant frequency, whereas the weave is reflected if its frequency is far from the resonance of the FSS. Moreover, the reflection and transmission properties depend on the angle of incidence.

By placing a FSS near to a PEC ground plane, the structure shows an high impedance in a very narrow band. This property is exploited to realize artificial High-Impedaance surface (HIS), based on a metallic two dimensional lattice place on a dieletric layer backed with a PEC ground plane.

EBG surface is the microwave analogue of the Photonic Bandgap (PCB) which operates in the visible band od the spectrum. An EBG surface is a structure which prevent the propagation of electromagnetic waves in a specific band of frequencies (gap) in the microwave region of the EM spectrum. The main feature of these materials is the existence of a gap (stopband) in the frequency spectrum of propagating EM waves. By considering a planar incident wave, the reflection phase of an EBG varies with frequency.

Consider a FSS placed on a PEC-backed substrate layer. The input impedance of such a structure can be seen as the parallel between the FSS impedance and the equivalent input impedance of the grounded dielectric slab.

$$Z_R = \frac{Z_d Z_{FSS}}{Z_d + Z_{FSS}}$$

When the imaginary part of the FSS impedance

$$Z_{FSS} = R - j\left(\frac{1-\omega^2 LC}{\omega C}\right)$$

and the inductive impedance of the substrate

$$Z_d = jZ_m^{TE,TM} tan(\beta d)$$

assume the same value, the parallel circuit resonates and the impedance Z_R of the structure is purely real. In order to obtained an absorption of an incoming wave, the impedance must match the free space impedance ζ_0.

One of the most interesting characteristic of some of EBG structures is that they can be design to act as Artificial Magnetic Conductor (AMC) surface. Some solutions are to use a periodic patch with vias, or a planar periodic FSS without vias. An AMC is a surface which simulates a perfect magnetic conductor and it has a reflectivity $\Gamma = +1$ (differently by the PEC which is -1). The AMC is characterized by a frequency such that the phase of the reflection coefficient is zero. The geometric complexity of the EBG structures makes very difficult the definition of analytic method to describe the performance, and thus to define design formula. EBG analysis exploits numerical techniques like methods of moments or full wave simulators based on advanced numerical methods. From the design point of view, the lack of analytic formula implies that the synthesis of EBG requests the integration of these numerical methods with an optimization algorithm, like Particle Swarm Optimization [20] or Genetic Algorithm [87].

Typical applications of these structures are thin electromagnetic absorber, coatings, or antenna designs. For instance, by aligning the resonant frequency of the antenna with the band gap of the EBG surface is possible to improve the antenna performance and reduce the surface wave in the substrate. However, the AMC behavior of these particular EBG structures exists only in a very narrow bandwidth around the resonance. This narrow-band limitation can severely restrict the number of useful applications for conventional passive AMC surfaces, especially when considered for antenna applications. A particular application of such a structure is to design ferrite metamaterials to mimic the properties of an effective magnetic conductor. Conventional ferrite materials have been large studied in last decades. One of the main problems of these materials is their performance degradation at frequencies above 1 GHz.

It has been demonstrate that an EBG built with an Frequency Selective Surface can be designed to work as a magnetic material over a PEC slab, with a frequency dependent permeability.

Through a proper technique of design (optimization), it is possible to synthesize almost any desired value of complex permeability, even negative.

19 Design

A proper optimization of the design parameters of a planar HZ-FSS structures provide the synthesis of metaferrites with any desired loss and either positive or negative values of $Re\{\mu\}$. This allows the application of metaferrites in the design of low loss left-handed or double-negative media.

To evaluate the magnetic performance of the EBG, it is necessary an equivalence between the metamaterial and the hypothetical homogeneous material we want to simulate. Kern and Werner [88] proposed a model based on the input impedance equivalence between the two models: an EBG structure characterized by a permittivity $\epsilon_r = \epsilon'_r - j\epsilon''_r$ and a thickness h and an hypothetical ferrite material slab placed on a PEC layer with permeability $\mu_r = \mu'_r - j\mu"_r$, permittivity $\epsilon_r = 1$ and a thickness d.

By representing the EBG with a parallel RLC equivalent circuit, and said respectively R,L,C the equivalent resistance, inductance and capacitance of the surface, the surface impedance seen by a normal incident wave on the EBG is

$$Z_s = R_s + jX_s = \omega L \left(\frac{A}{A^2 + B^2} + j \frac{B}{A^2 + B^2} \right)$$

with

$$A = \frac{\omega L}{R} \qquad B = 1 - \left(\frac{\omega}{\omega_0} \right)^2 \qquad \omega_0 = \frac{1}{\sqrt{LC}}$$

As regards the PEC backed slab of magnetic material, the surface impedance has the same form of the input impedance of a open circuit stub

$$Z_s = jZ_0 tg(k_0 \mu_r d) \qquad with \qquad Z_0 = \zeta_0 \sqrt{\mu_r}$$

By equating the two expressions

$$R_s + jX_s = j\zeta_0 \sqrt{\mu'_r - j\mu"_r} tg \left(j\beta_0 \sqrt{\mu'_r - j\mu"_r} d \right)$$

if the magnetic slab is sufficiently this, it is possible approximate the tangent with its argument. This exemplification leads to the design equations for the equivalent permeability of the EBG structure

$$\mu'_r = \frac{X_s}{\zeta_0 k_0 d} \tag{68}$$

$$\mu"_r = \frac{R_s}{\zeta_0 k_0 d} \tag{69}$$

To evaluate the magnetic performance of the EBG as metaferrite, it has been necessary a connection between the CAD used to simulate the structure, Ansoft HFSS, and Matlab. This

connection between the software han been realized by using a Visual Basic script: the Matlab code generate a VBS script which describe the geometry, this is sent to HFSS which evaluate the scattering parameters of the project and send them to Matlab, which extrapolates from them the effective permeability of the metamaterial. Figure 52 explains this connection

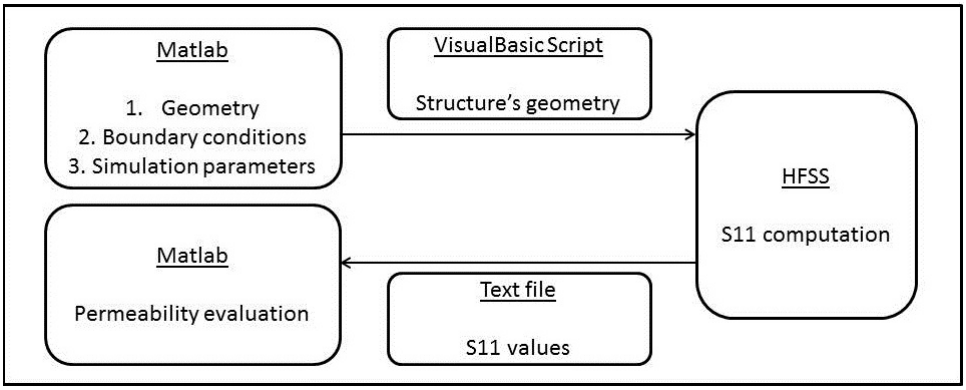

Figure 52: Top view of the metaferrite unit cell

To demonstrate the effectiveness of this technique, it has been simulated a metaferrite proposed in [87] and evaluated by the author trough the Method of Moments, whose FSS screen geometry is shown in figure 53

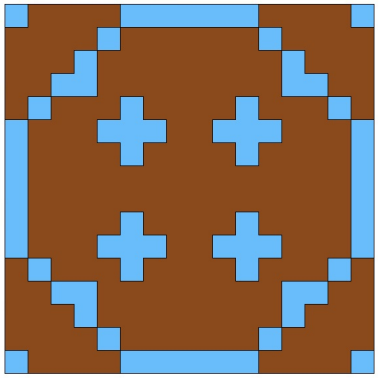

Figure 53: Top view of the metaferrite unit cell

The following graphs reports the results obtained by Kern and by our Matlab-HFSS tests, shown in figure 54, and show a good agreement, except for a resonance frequency shift. The permeability at the frequency $f = 1.575GHz$ is $\mu = 12.73 + i0.003974$

This geometry has been studied to evaluate the effects of various parameters of the model on the magnetic behaviour of the structure, like the dielectric thickness, the values of the dielectric constant of the substrate and angle of incidence of the incident wave. The figure 55

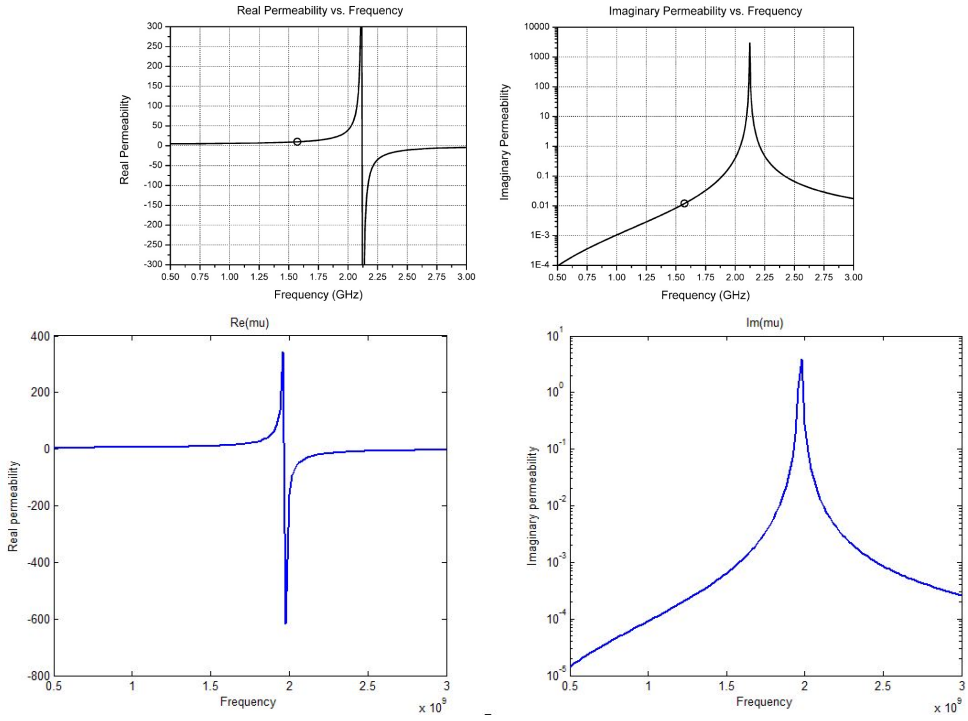

Figure 54: Permeability of the metaferitte under test

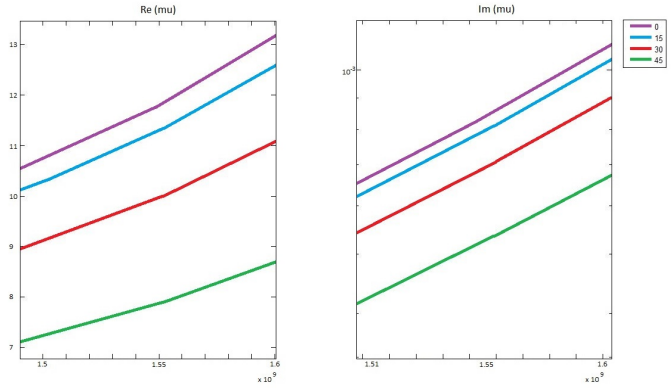

Figure 55: Permeability as a function of the angle of incidence

shows how the equivalent permeability is maximum for a normal incidence and decreases as the angle of incidence increases. This aspect must be taken into account in the metaferrite design for particular applications, as antenna substrate. The field lines under the edges of the patch are not normal to this , but they are curvilinear. So the substrate placed in this position has a different magnetic performance compared to the substrate under the center of the antenna.

20 Optimization

The optimization involves the same PSO algorithm implemented for the ridges described in the previous chapters of this thesis, but this time it has been connected to HFSS which provide the return loss values in order to evaluate the fitness values, as shown in fig. 3. The variables to be optimized by the algorithm are the geometry of the screen, the heights and the dielectric constant of the substrates. The screen is designed to achieve eight-fold symmetric unit cell, which provide the same response for both TE and TM waves, and simplifies the solution space.

As a proof of the technique effectiveness, a HZ-FSS structure with the resonance at 4

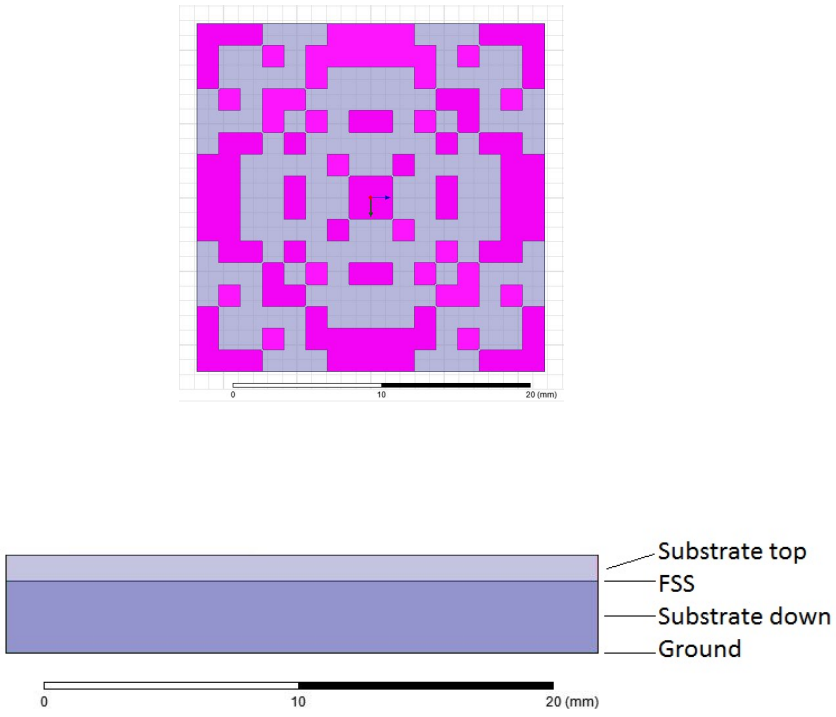

Figure 56: Geometry of the optimized cell

GHz has been optimized. The geometry consists of a two dielectric layers and a FSS put between of them. The optimized geometry is show in figures 56 and the optimized parameters are in table 23. Figure 57 show the performance in terms of phase: the resonant results to be very near to 4 GHz.

Cell unit size	23.6mm
Top substrate height	1.04 mm
Top substrate permeability	12.3 - j 0.0116
Bottom substrate height	2.87mm
Bottom substrate permeability	2.03 - j 0.002

Table 23: Parameters of the optimized structure

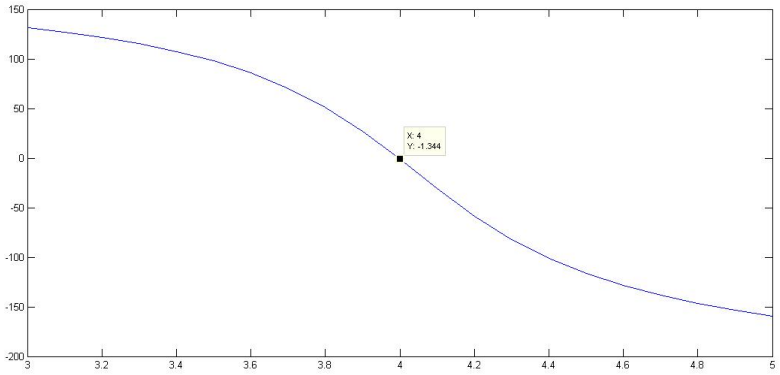

Figure 57: Phase diagram of the optimized cell

Part VI

Conclusions

Aim of this thesis is to study the application of the optimization technique to different topics of the microwave engineering. It has been shown that the Particle Swarm Optimizations is suitable for such a purpose, and it can be combined with several numerical techniques or connected to CAD software to achieve the performance evaluations. In particular, the PSO allows to obtained the optimal configuration of the device even if it is requested a trade-off between conflicting requirements.

As regards the numerical techniques, in this work different versions of the FDFD technique have been developed and applied to the ridge waveguide design and optimization. FDFD provides a very accurate representation of the structure with an high computational load compared to the traditional CADS based on the finite element methods.

Moreover, the connection of a Matlab optimization code with the typical commercial CADs as CST and HFSS has been applied to the design of resonant cavities, waveguide impedance transformators and particular metamaterials.

All the cases have proved the efficiency of the PSO in microwave device optimization.

Part VII

List of Publications

Alessandro Fanti, Marco Simone, Giuseppe Mazzarella

Hight order FD computation of TE and TM modes in single grid

Progress in Electromagnetics Research Symposium,

PIERS 2013 Stockholm; Stockholm; Sweden; 12-15 August 2013; Pages 1224-1227

Alessandro Fanti, Marco Simone, Giuseppe Mazzarella

High Order FDFD computation of all waveguide modes using a single grid

2013 Loughborough Antennas and Propagation Conference,Loughborough, Leicestershire, UK

11-12 November 2013, Article number 6711855, Pages 74-77

Marco Simone, Alessandro Fanti, Giuseppe Mazzarella

Optimization of rectangular ridge waveguides using PSO

2013 Loughborough Antennas and Propagation Conference,Loughborough, Leicestershire, UK

11-12 November 2013, Article number 6711855, Pages 74-77

Marco Simone, Alessandro Fanti, Giuseppe Mazzarella, Giorgio Montisci

Band Optimization of Ridge Waveguides Using PSO,

Proceedings of IEEE, The 30th Annual Review of Progress in Applied Computational Electromagnetics, ACES 2014, March 23 – 27, 2014, Jacksonville, Florida

Marco Simone, Alessandro Fanti, Giorgio Montisci , Giovanni Andrea Casula,and Giuseppe Mazzarella

Combined PSO-FDFD Optimization of Rectangular Ridged Waveguides

ACES Journal, Vol. 31, No. 2 , 2016

Marco Simone, Alessandro Fanti, Giuseppe Mazzarella

Ridge waveguide optimization with PSO algorithm

Journal of Electromagnetic Waves and Applications

Volume 29, Issue 2, 22 January 2015, Pages 199-209

Alessandro Fanti, Sergio Casu, Francesco Desogus, Giorgio Montisci, Marco Simone, Giovanni Andrea Casula, Paolo Maxia, Giuseppe Mazzarella, Renzo Carta

Evaluation of a microwave resonant cavity as a reactor for enzyme reactions Journal of Electromagnetic Waves and Applications

Volume 29, Issue 17, November 2015, pages 2380-2392

Part VIII

Bibliography

References

[1] Alessandro Fanti, Marco Simone, Giuseppe Mazzarella
Hight order FD computation of TE and TM modes in single grid
Progress in Electromagnetics Research Symposium,
PIERS 2013 Stockholm; Stockholm; Sweden; 12-15 August 2013; Pages 1224-1227

[2] Alessandro Fanti, Marco Simone, Giuseppe Mazzarella
High Order FDFD computation of all waveguide modes using a single grid
2013 Loughborough Antennas and Propagation Conference,Loughborough, Leicestershire, UK
11-12 November 2013, Article number 6711855, Pages 74-77

[3] Marco Simone, Alessandro Fanti, Giuseppe Mazzarella, Giorgio Montisci
Band Optimization of Ridge Waveguides Using PSO,
Proceedings of IEEE, The 30th Annual Review of Progress in Applied Computational Electromagnetics, ACES 2014, March 23 – 27, 2014, Jacksonville, Florida

[4] Marco Simone, Alessandro Fanti, Giuseppe Mazzarella
Optimization of rectangular ridge waveguides using PSO
2013 Loughborough Antennas and Propagation Conference,Loughborough, Leicestershire, UK
11-12 November 2013, Article number 6711855, Pages 74-77

[5] Marco Simone, Alessandro Fanti, Giorgio Montisci , Giovanni Andrea Casula,and Giuseppe Mazzarella
Combined PSO-FDFD Optimization of Rectangular Ridged Waveguides

Accepted on ACES Journal

[6] Marco Simone, Alessandro Fanti, Giuseppe Mazzarella
Ridge waveguide optimization with PSO algorithm
Journal of Electromagnetic Waves and Applications, Volume 29, Issue 2, 22 January 2015, Pages 199-209

[7] Beni, G., Wang, J.
Swarm Intelligence in Cellular Robotic Systems,
Proceed. NATO Advanced Workshop on Robots and Biological Systems, Tuscany, Italy, June 26–30 (1989)

[8] Kennedy, Eberhart
Particle Swarm Optimization
IEEE International Conference on Neural Networks, 1995. Proceedings, (Vol. 4)

[9] Eberhart, Kennedy
A new optimizer using particle swarm theory
Proceedings of the Sixth International Symposium on Micro Machine and Human Science, 1995. MHS '95., pp 39-43

[10] Shi, Eberhart
A modified Particle Swarm Optimizer
The 1998 IEEE International Conference on Evolutionary Computation Proceedings, 1998. IEEE World Congress on Computational Intelligence., pp.69 - 73

[11] Shi, Eberhart
Empirical study of Particle Swarm Optimization
Proceedings of the 1999 Congress on Evolutionary Computation, 1999. CEC 99.

[12] H. R. Li, Y. L. Gao

Particle Swarm Optimization Algorithm with Exponent Decreasing Inertia Weight and Stochastic Mutation

Information and Computing Science, 2009. ICIC '09. Second International Conference on (Volume:1), pp. 66 - 69

[13] Huang Chongpeng, Zhang Yuling, Jiang Dingguo, Xu Baoguo

On Some Non-linear Decreasing Inertia Weight Strategies in Particle Swarm Optimization

Proceedings of the 26th Chinese Control Conference July 26-31, 2007, Zhangjiajie, Hunan, China, pp. 750-753

[14] Said M. Mikki and Ahmed A. Kishk,

Hybrid Periodic Boundary Condition for Particle Swarm Optimization,

IEEE Transactions on Antennas and Propagation, suppl. 255.11 (2007)

[15] Jacob Robinson and Yahya Rahmat-Samii,

Particle Swarm Optimization in Electromagnetics,

IEEE Transactions on Antennas and Propagation, vol. 52, no. 2, February 2004

[16] M. Ferndandez Pantoja, A. Rubio Bretones, F. Garcia Ruiz, S. G. Garcia; R Gomez Martin

Particle-Swarm Optimization in Antenna Design: Optimization of Log-Periodic Dipole Arrays,

IEEE Antennas and Propagation Magazine 49.4 (2007).

[17] Nanbo Jin, Yahya Rahmat-Samii

Hybrid Real-Binary Particle Swarm Optimization (HPSO) in Engineering Electromagnetics,

IEEE Transactions on Antennas and Propagation, vol. 58, n0. 12, December 2010

[18] Nanbo Jin, Yahya Rahmat-Samii
Parallel Particle Swarm Optimization and Finite-Difference Time-Domain (PSO/FDTD) Algorithm for Multiband and Wide-Band Patch Antenna Designs
IEEE Transactions on Antennas and Propagation, vol. 53, no. 11, November 2005

[19] Shenheng Xu, Yahya Rahmat-Samii, and Dennis Gies,
Shaped-reflector antenna designs using particle swarm optimization: an example of a direct-broadcast satellite antenna,
Microwave and Optical Technology Letters Volume 48, Issue 7, pages 1341–1347, July 2006

[20] N. Jin, Y. Rahmat-Samii,
Parallel PSO/FDTD Algorithm for the Optimization of Patch Antennas and EBG Structures ,
IEEE/ACES International Conference on Wireless Communications and Applied Computational Electromagnetics, 2005.

[21] Jin, N., Rahmat-Samii, Y.,
Advances in particle swarm optimization for antenna designs: real-number, binary, single-objective and multiobjective implementations,
IEEE Transactions on Antennas and Propagation, 2007, 55, 3, part 1 556–567

[22] S. Xu, Y. Rahmat-Samii, and D. Gies,
Shaped-reflector antenna designs using particle swarm optimization: an example of a direct-broadcast satellite antenna,
Microwave and Optical Technology Letters Volume 48, Issue 7, pages 1341–1347, July 2006

[23] Yan-Liang Li, Wei Shao, Long You, and Bing-Zhong Wang,
An Improved PSO Algorithm and Its Application to UWB Antenna Design

IEEE Antennas and Wireless Propagation Letters, VOL. 12, 2013

[24] S. Genovesi, R. Mittra, A. Monorchio, G. Manara,
Particle Swarm Optimization for the Design of Frequency Selective Surfaces,
IEEE Antennas and Wireless Propagation Letters, VOL. 5, 2006

[25] S.K. Goudos, Z.D. Zaharis, M. Salazar-Lechuga, P. I. Lazaridis and P. B. Gallion
Dielectric filter optimal design suitable for microwave communications by using multiobjective evolutionary algorithms,
Microwave and Optical Technology Letters, Volume 49, Issue 10, pages 2324–2329, October 2007

[26] S. K. Goudos and J. N. Sahalos
Microwave absorber optimal design using multi-objective particle swarm optimization,
Microwave and Optical Technology Letters, Volume 48, Issue 8, pages 1553–1558, August 2006

[27] Cohn S.B.,
Properties of ridgeguided waves.,
Procedings of the I.R.E., August 1947;783–788.

[28] Hopfer S.,
The Design of Ridge Waveguide
IEE Transaction on Microwave Theory and Techiniques 3; 1955. p. 20-29

[29] Sorrentino R.,
Transverse Resonance Technique.
In: T. Itoh (Ed.) Numerical Techniques for Microwave and Millimetre Wave Passive Structures, Ch. 11, pp.637-696, John Wiley, New York, 1989.

[30] Helszajn J., McKay M.
Voltage-current definition of impedance of double ridge waveguide using the finite element method,
Microwaves, Antennas and Propagation, IEE Proceedings (Volume:145 , Issue: 1), February 1998.

[31] A. Fanti and G. Mazzarella,
Curvilinear Finite Difference Approach to the Computation of Modes of Circular and Elliptic Waveguides
IEEE Proc. Int. Conf. on Applied Electromagnetics and Communications, (ICECom 2010), Dubrovnik, Croazia, 20-23 September 2010.

[32] A. M, Svedin,
Propagation analysis of chiro waveguides using the finite element method,
IEEE Trans. on Microwave Theory Tech., vol. 38, no. 10, pp.1488-1496, Oct. 1990

[33] Collin,
Field Theory of Guided Waves
IEEE Press, 2nd ed, New York, 1991.

[34] L. J. Chu,
Electromagnetic waves in elliptic hollow pipes of metal,
Journal of Applied Physics, Vol. 9, pp. 583-591, September 1938.

[35] N. Marcuvitz,
Waveguide Handbook,
Peregrinius, London, 1986.

[36] J. G. Kretzschmar,
Wave propagation in hollow conducting elliptical waveguides,

IEEE Transactions on Microwave Theory and Techniques, Vol. 18, Issue (9), pp. 547-554, September 1970.

[37] D. L. Young, S. P. Hu, C. W. Chen, C. M. Fan and K. Murugesan
Analysis of elliptical waveguides by the method of fundamental solutions,
Microwave and Optical Technology Letters, Vol. 44, pp. 552 -558, February 2005.

[38] G. P. Zouros
Exact cutoff wave numbers of composite elliptical metallic waveguides",
IEEE Transactions on Microwave Theory and Techniques, Vol. 61, Issue (9), pp.3179 -3186, September 2013

[39] Das, Sanyal,
Coaxial-to-waveguide transition (end-launcher type),
PROC. IEE, Vol. 123, No. 10, OCTOBER 1976

[40] Collin,
Theory and Design of Wide-Band Multisection Quarter-Wave Transformers,
Proceedings of the IRE, 1955

[41] Deshpande, Das, Sanyal,
Analysis of an End Launcher for an X-Band Rectangular Waveguide,
IEEE Transactions on Microwave Theory and Techniques, VOL. MTr-27, NO. 8, AUGUST 1979

[42] Wheeler,
Broadband waveguide-to-coax transitions,
1958 IRE International Convention Record, VOL. 5

[43] Tang, Wong,
Multimode Phased Array Element for Wide Scan Angle Impedance Matching,
Proceedings of the IEEE, November 1968

[44] Dix,
Design of waveguide/caoxial transition for the band 1.5-4.1 Gc/s,
Proceedings of the IEEE, Vol 110, No.2, February 1963

[45] Hui-Wen Yao, Am Abdelmonem, Ji-Fuh Liang, Kawthar A. Zaki,
Analysis and Design of Microstrip-to-Waveguide Transitions,
IEEE Transactions on Microwave Theory and Techniques. VOL. 42, NO. 12, DECEMBER 1994

[46] Dominic Deslandes, Ke Wu,
Integrated Microstrip and Rectangular Waveguide in Planar Form,
IEEE Microwave and Wireless Components Letters, VOL. 11, NO. 2, FEBRUARY 2001

[47] Zhang, Ruiz-Cruz, Zaki, Piloto
A Waveguide to Microstrip Inline Transition With Very Simple Modular Assembly
IEEE Microwave and Wireless Components Letters, VOL. 20, NO. 9, SEPTEMBER 2010

[48] Helszajn J.
Ridge waveguides and passive microwave components
IEE, UK, 2000

[49] Fanti A., Mazzarella G.,
Finite Difference Polar-Cartesian Grid Approach For Mode Computation in Rounded-End Waveguides,
Applied Computational Electromagnetics Society (ACES) Journal, vol.26, no. 9,

pp.768-775, September 2011

[50] Svedin, J.A.M.
Propagation analysis of chirowaveguides using the finite element method,
IEEE Trans. on Microwave Theory Tech., vol. 38, no. 10, pp.1488-1496, Oct. 1990.

[51] Fanti A., Montisci G., Mazzarella G., Casula G.A.
VFD Approach to the Computation TE and TM Modes in Elliptic Waveguide on TM Grid,
Applied Computational Electromagnetics Society Journal 28(12):1205-1212 · DECEMBER 2013

[52] Kennedy J., Eberhart R.,
Particle swarm optimization.,
Proceedings of IEEE International Conference on Neural Networks, vol. 4, pp. 1942–1948, Perth, Wash, Australia, Nov.1995

[53] Robinson J., Rahmat-Samii Y.
Particle swarm optimization in electromagnetics
IEEE Transactions on Antennas and Propagation, vol. 52, no. 2, pp. 397–407, 2004.

[54] Jin N., Rahmat - Samii Y.
Particle Swarm Optimization for Antenna Designs in Engineering Electromagnetics
Journal of Artificial Evolution and Applications, Volume 2008

[55] Rogovich A., Marasini C., Monorchio A., Lepelaars E. S. A. M., Zwamborn A. P. M.
Design of Wire Antennas by Using an Evolved Particle Swarm Optimization Algorithm
International Conference on Electromagnetics in Advanced Applications. ICEAA 2007.

[56] Choukiker Y., Behera S. K., Mishra D., Mishra R. K.
Optimization of Dual Band Microstrip Antenna Using PSO
Applied Electromagnetics Conference 2009, pp. 1-4, December 2009.

[57] Fanti A., Mazzarella G., Montisci G., Casula G. A.
Computation of the modes of elliptic waveguides with a curvilinear 2D Frequency-Domain Finite-Difference Approach
Progress In Electromagnetics Research M, vol. 26, pp 69–84, 2012

[58] Eberhart R.C., Shi Y.
Particle swarm optimization: developments, applications and resources
Proceedings of the 2001 Congress on Evolutionary Computation, 2001. (Volume:1)

[59] Xu F., Jiang X., Wu K.
FDFD Modeling of substrate integrated waveguide without phase-bias
Proc. 35th Eur. Micr. Conf., pp 853–056, 2005

[60] Fanti A., Mazzarella G., Montisci G.
Curvilinear Vector Finite Difference Approach to the Computation of Waveguide Modes
Advanced Electromagnetics Journal, ISSN: 2119-0275, Vol.1, May 2012.

[61] Y. J. Zhao, K. L. Wu, and K. K. M. Cheng
A compact 2–D full–wave finite–difference frequency–domain method for general guided wave structures, IEEE
Trans. Microwave Theory Techniques, Vol. 50, pp- 1844–1848, 2002.

[62] G. Mazzarella and G. Montisci
Accurate Characterization of the Interaction between Coupling Slots and Waveguide Bends in Waveguide Slot Arrays

IEEE Trans. Microw. Theory Tech., vol. MTT–48, pp. 1154- 1157, Sep. 2000.

[63] T. Hirano , J. Hirokawa and M. Ando
Method of moments analysis of a waveguide crossed slot by using the eigenmode basis functions derived by the edge-based finite-element
Proc. Inst. Elect. Eng. Microwaves, Antennas Propagation, vol. 147, no. 5, pp.349 -353, 2000

[64] Bornemann J., Taringou F.
Mode-matching analysis of substrate-integrated waveguide circuits,
Proc. Canadian Conf. Elec. Comp. Engr., pp. 579-582, Niagara Falls, Canada, May 2011.

[65] Morton K.W.,
Mayers D.F. Numerical Solution of Partial Differential Equations, An Introduction,
Cambridge University Press, 2005.

[66] A. Fanti, M. Simone and G. Mazzarella,
High Order FDFD Computation of all Waveguide Modes using a Single Grid,
IEEE, Int. Proc. 2013 Loughborough Antennas and Propagation Conference ,Loughborough, UK, 2013.

[67] Foster KR.,
Thermal and nonthermal mechanisms of interaction of radio-frequency energy with biological systems,
IEEE Transactions on Plasma Science, Vol. 28, Issue 1 , 2000

[68] O.P. Gandhi, G. Lazzi, C.M. Furse,
Electromagnetic absorption in the human head and neck for mobile telephones at 835 and 1900 MHz

IEEE Transactions on Microwave Theory and Techniques, Vol. 44 , Issue: 10 , 1996

[69] Hidenori Akiyama, Takashi Sakugawa, Takao Namihira, Koichi Takaki, Yasushi Minamitani, Naoyuki Shimomura
Industrial Applications of Pulsed Power Technology
IEEE Transactions on Dielectrics and Electrical Insulation Vol. 14, No. 5; October 2007

[70] Xingfeng Guo, Dongmei Han, Huping Xi, Lei Rao, Xiaojun Liao, Xiaosong Hu, Jihong Wu *Extraction of pectin from navel orange peel assisted by ultrahigh pressure, microwave or traditional heating: a comparison*
Carbohydrate Polymers, Volume 88, Issue 2, 2 April 2012, Pages 441–448

[71] Kirat Rawal, Manish Kumar Mishra, , Manish Dixit, Meka Srinivasarao
Microwave assisted solvent free synthesis of α-α'-bis (arylidene) cycloalkanones by sulfated zirconia catalyzed cross aldol condensation of aromatic aldehydes and cycloalkanones
Journal of Industrial and Engineering Chemistry, Volume 18, Issue 4, 25 July 2012, Pages 1474–1481

[72] Fanny Monteil-Rivera, Louise Paquet
Solvent-free catalyst-free microwave-assisted acylation of lignin
Industrial Crops and Products, Vol 65, pp. 446-453 · March 2015

[73] György Keglevich, Erika Bálint, Éva Karsai, Alajos Grün, Mária Bálint, István Greiner
Chemoselectivity in the microwave-assisted solventfree solid-liquid phase benzylation of phenols: O- versus C-alkylation
Tetrahedron Letters, Volume 49, Issue 34, 18 August 2008, Pages 5039–5042

[74] Carta R, Desogus F.
The effect of low-power microwaves on the growth of bacterial populations in a plug fow reactor
AIChE Journal, Vol. 56, Issue 5,Pages 1270–1278 , May 2010

[75] Carta R, Desogus F, Errico M.
Effect of microwave radiation on the growth rate of Bacillus clausii at 37°C
CHISA 2006 – 17th International Congress of Chemical and Process Engineering; 2006 Aug 27–31; Prague, Czech Republic, code 70283.

[76] Carta R, Desogus F.
The enhancing effect of low power microwaves on phenol oxidation by the Fenton process
Journal of Environmental Chemical Engineering, Volume 1, Issue 4, December 2013, Pages 1292–1300

[77] Asher Shazman, Shimon Mizrahi, Uri Cogan, Eyal Shimoni
Examining for possible non-thermal effects during heating in a microwave oven
Food Chemistry, Vol. 103, Issue 2, 2007, Pages 444–453.

[78] Neelancherry Remya , Jih-Gaw Lin
Current status of microwave application in wastewater treatment – a review
Chemical Engineering Journal, Vol. 166, Issue 3, 1 February 2011, Pages 797–813

[79] Fei Zuo, Alexandre Badev, Sébastien Saunier, Dominique Goeuriot, Romain Heuguet, Sylvain Marinel
Microwave versus conventional sintering: estimate of the apparent activation energy for densification of α-alumina and zinc oxide
Journal of the European Ceramic Society, Volume 34, Issue 12, October 2014, Pages 3103–3110

[80] Dahai Yu, , Hao Wu, Aijun Zhang, Li Tian, Ludong Liu, Chuanming Wang, Xuexun Fang
Microwave irradiation-assisted isomerization of glucose to fructose by immobilized glucose isomerase
Process Biochemistry, Vol. 46, Issue 2, February 2011, Pages 599–603

[81] Alfred K. Anderson, Harmeet S. Guraya
Effects of microwave heat-moisture treatment on properties of waxy and non-waxy rice starches
Food Chemistry, Volume 97, Issue 2, July 2006, Pages 318–323

[82] Patrícia Caroline Molgero Da Rós, William Costa e Silva, Daniel Grabauskas, Victor Haber Perez, Heizir Ferreira de Castro
Biodiesel from babassu oil: Characterization of the product obtained by enzymatic route accelerated by microwave irradiation
Industrial Crops and Products, Volume 52, January 2014, Pages 313–320

[83] M.R. Avhad, J.M. Marchetti, *A review on recent advancement in catalytic materials for biodiesel production*
Renewable and Sustainable Energy Reviews, Volume 50, October 2015, Pages 696–718

[84] Guifen Gonga, Danyu Liub, Yudong Huang *Microwave-assisted organic acid pretreatment for enzymatic hydrolysis of rice straw*
Biosystems Engineering, Volume 107, Issue 2, October 2010, Pages 67–73

[85] Harrington RF
Time-harmonic electromagnetic fields
New York (NY): McGraw-Hill; 1961

[86] Zajìček R, Oppl L, Vrba J.
Broadband measurement of complex permittivity using reflection method and coaxial probes
Radio Eng. 2008;17:14–19

[87] Douglas J. Kern, Douglas H. Werner, Agostino Monorchio, Luigi Lanuzza, and Michael J. Wilhelm
The Design Synthesis of Multiband Artificial Magnetic Conductors Using High Impedance Frequency Selective Surfaces,
IEEE Transactions on Antennas and Propagation, vol. 53, NO. 1, January 2005

[88] Douglas J. Kern, Douglas H. Werner, Mikhail Lisovich,
Metaferrites: Using Electromagnetic Bandgap Structures to Synthesize Metamaterial Ferrites,
IEEE Transactions on Antennas and Propagation, vol. 53, no. 4, April 2005



Part IX

Acknowledgements

I really like to thank all the people who have supported me during these last 3 years.

Thanks to my family for the great support I received till now, and to all my friends with whom I spent a good time of fun and laughs.

I would like to thank my tutor Prof. Giuseppe Mazzarella who supervised my work during this period. A special thanks to Dr. Alessandro Fanti for his valuable help along these years. Thanks to Prof. Giorgio Montisci and all the electromagnetic group, and to the students who spent a piece of time in the laboratory during these years, especially Nicola, Claudio, Paolo, Riccardo, Sergio, Giacomo and Gianluca.

Moreover, thanks to the group of the Selargius astronomical observatory for the period I spent in their laboratories, especially to Giuseppe Valente for his help.

Finally, thanks to the Antenna and Electromagnetic group of the Queen Mary University of London, where I spent 6 months of my study. I would like to thank Prof. Yang Hao who gave me the opportunity of standing in his group for 6 months and moreover offered me a contract as post-doctoral researcher assistant, my current employment. Thanks to Luigi for his great help to enter the new group and overcome the difficulties I faced. Thanks also to the other guys I met in this 6 months, Ben, Maijid and Darryl, and all the rest of the group.



Marco Simone gratefully acknowledges Sardinia Regional Government for the financial support of his PhD scholarship (P.O.R. Sardegna F.S.E. Operational Programme of the Autonomous Region of Sardinia, European Social Fund 2007- 2013 - Axis IV Human Resources, Objective l.3, Line of Activity l.3.1.).